

Contribution of changes in atmospheric circulation patterns to extreme temperature trends

Daniel E. Horton^{1,2*}, Nathaniel C. Johnson^{3,4,5}, Deepti Singh¹, Daniel L. Swain¹, Bala Rajaratnam^{1,2,6}, and Noah S. Diffenbaugh^{1,2}

¹Department of Earth System Science, Stanford University, Stanford, CA 94305, USA

²Woods Institute for the Environment, Stanford University, Stanford, CA 94305, USA

³International Pacific Research Center, University of Hawaii at Manoa, Honolulu, HI 96822, USA

⁴Scripps Institution of Oceanography, University of California San Diego, La Jolla, CA 92093, USA

⁵Cooperative Institute for Climate Science, Princeton University, Princeton, NJ 08540, USA

⁶Department of Statistics, Stanford University, Stanford, CA, 94305, USA

*Corresponding author. Email: danethan@stanford.edu

Contribution of changes in atmospheric circulation patterns to extreme temperature trends

1 Surface weather conditions are closely governed by the large-scale
2 circulation of the atmosphere. Recent increases in the occurrence of some extreme
3 weather phenomena^{1,2} have led to multiple mechanistic hypotheses linking changes
4 in atmospheric circulation to increasing extreme event probability³⁻⁵. However,
5 observed evidence of long-term change in atmospheric circulation remains
6 inconclusive⁶⁻⁸. Here we identify statistically significant trends in the occurrence of
7 mid-atmospheric circulation patterns, which partially explain observed trends in
8 surface temperature extremes over seven mid-latitude regions of the Northern
9 Hemisphere. Utilizing self-organizing map (SOM) cluster analysis⁹⁻¹², we detect
10 robust pattern trends in a subset of these regions during both the satellite
11 observation era (1979–2013) and the recent period of rapid Arctic sea ice decline
12 (1990–2013). Particularly substantial influences include the contribution of
13 increasing trends in anticyclonic circulations to summer/autumn hot extremes over
14 portions of Eurasia and North America, and the contribution of increasing trends in
15 northerly flow to winter cold extremes over central Asia. Our results indicate that
16 although a substantial portion of the observed change in extreme temperature
17 occurrence has resulted from regional- and global-scale thermodynamic changes,
18 the risk of extreme temperatures over some regions has also been altered by recent
19 changes in the frequency, persistence, and/or maximum duration of regional
20 circulation patterns.

21 Although most land regions show robust warming over the past century¹³, the
22 pattern of change has not been spatially uniform¹⁴. This heterogeneity results from
23 regional differences in the response of the climate system to increasing radiative forcing,
24 and from the background noise of climate variability. Together, these factors
25 substantially increase the challenge of climate change detection, attribution, and
26 projection at regional and local scales^{14,16}.

27 The spatial pattern of changes in extreme weather events has generated arguments
28 that global warming has caused dynamic and/or thermodynamic changes that have
29 differentially altered extreme event probabilities^{1,17}. Thermodynamic arguments are well

30 understood and observed. For example, the accumulation of heat in the atmosphere has
31 resulted in upward trends in hot extremes, downward trends in the majority of cold
32 extremes, and more intense hydroclimatic events^{1,2}. Dynamic arguments have greater
33 uncertainties¹⁵⁻¹⁹. Changes in the large-scale atmospheric circulation – for instance, an
34 increase in the occurrence or persistence of high-amplitude wave patterns – could alter
35 the likelihood of extreme events²⁰. Recent extremes in the Northern Hemisphere mid-
36 latitudes^{1,2,17} have motivated hypotheses of a dynamic linkage between “Arctic
37 Amplification”, altered atmospheric circulation patterns, and changes in the probability of
38 mid-latitude extremes^{e.g.,3-5,17}. Despite divergent views on the causal direction of this
39 linkage¹⁷, altered atmospheric dynamics are consistently invoked. Although trends in
40 mean-seasonal mid-atmospheric geopotential height anomalies have been identified (Fig.
41 2.36 ref. 21; Fig. 1), evidence of changes in the occurrence of sub-seasonal atmospheric
42 patterns remains equivocal, as does their contribution to extreme event probabilities⁶⁻⁸.

43 Previous efforts to detect trends in atmospheric circulation may have been
44 hampered by narrowly-defined, spatially-sensitive, and/or non-standardized metrics^{3,6-8,17}.
45 We therefore employ a large-scale spatial characterization approach – Self-Organizing
46 Map (“SOM”) cluster analysis – to track the occurrence of highly generalized mid-
47 atmospheric circulation patterns. We use 500 hPa geopotential height anomaly fields to
48 describe daily circulation, and group each day’s pattern into one of a predefined number
49 of SOM clusters based on a measure of pattern similarity⁹⁻¹² (Methods). The number of
50 clusters is largely dependent on the degree of specificity/generality required to test a
51 particular hypothesis⁹⁻¹². To facilitate generalized large-scale mid-atmospheric
52 classification, we utilize four clusters per domain. Using three reanalyses (NCAR/NCEP-
53 R1, NCEP-DOE-R2, and ERA-Interim), we calculate linear trends [yr^{-1}] in the time-
54 series of annual values of (i) the total number of days in each season on which each SOM
55 pattern occurs (“occurrence”; [$\text{d}\cdot\text{yr}^{-1}$]), (ii) the mean length of consecutive occurrence
56 (“persistence”; [$\text{d}\cdot\text{event}^{-1}$]), and (iii) the longest consecutive occurrence (“maximum
57 duration”; [$\text{d}\cdot\text{event}^{-1}$]). We consider trends in each metric robust if matching circulation
58 patterns from all three reanalyses have statistically significant trends of the same sign.
59 We assess the robustness of trends for seven mid-latitude regions (Fig. 2a), over both the
60 satellite era (1979–2013; “sat-era”) and the rapidly-diminishing Arctic sea ice era²²

61 (1990–2013; “ice-era”). We report circulation patterns that pass these robustness criteria,
62 but also discuss results in the context of (i) comprehensive multiple hypothesis testing,
63 (ii) removal of the assumption of linear time-series relationships, (iii) use of fewer/more
64 clusters, and (iv) addition of atmospheric thermal dilation controls (Methods; ED_Table 1
65 and ED_Figs. 1-3).

66 Of the 112 total circulation patterns analyzed in each period (Methods), the three
67 reanalyses exhibit statistically significant trends in pattern occurrence for a total of 17,
68 16, and 16 patterns in the sat-era, and 15, 13, and 14 patterns in the ice-era (ED_Table
69 1a). Of these significant occurrence trends, 12 sat-era and 10 ice-era patterns are robustly
70 significant across all three reanalyses (Table 1). The majority of robust sat-era trends
71 occur in summer and autumn, while robust ice-era trends are more evenly distributed
72 over summer, autumn, and winter. These patterns are diverse, and include anticyclonic,
73 cyclonic, and “dipole” circulations (ED_Figs. 4-5). Patterns with robust trends in both
74 sat- and ice-eras are limited to summer and autumn over western Asia and eastern North
75 America.

76 While the number of significant trends in pattern persistence varies from 5 to 10
77 across the individual reanalyses (ED_Table 1a), only three robust pattern persistence
78 trends are identified in each period (Table 1). Robust maximum duration trends are more
79 prevalent, including five in the sat-era and six in the ice-era. These are predominantly
80 associated with summer anticyclonic patterns, although the maximum duration of central
81 Asia winter troughing events demonstrates a robust ice-era increase (ED_Figs. 4-5). In
82 regions with robust trends in multiple patterns, those patterns are generally
83 complimentary. For example, in summer over eastern North America, robustly increasing
84 sat-era trends in anticyclonic patterns co-occur with robustly decreasing trends in
85 cyclonic patterns.

86 To what extent have mid-atmospheric circulation trends influenced the likelihood
87 of temperature extremes? For each period, we compute area-weighted trends in the
88 seasonal occurrence of temperature extremes for all days, and for those days associated
89 with each SOM pattern (e.g., Fig. 2a, j-m; Methods). The three reanalyses generally agree
90 on the direction of all-days trends: consistent with enhanced radiative forcing and global

91 warming, most regions and seasons show positive trends in hot occurrence, and negative
92 trends in cold occurrence (Table 1).

93 Hot extremes are projected to increase due to the dynamic and thermodynamic
94 effects of global warming^{1,23}. Consistent with other assessments^{1,2}, we find substantial
95 increases in extreme heat occurrence over the mid-latitudes (ED_Figs. 6-7). For instance,
96 the regional-mean occurrence of summer hot days over Europe, western Asia and eastern
97 North America has increased 0.10, 0.16, and 0.13 $\text{d}\cdot\text{yr}^{-1}\cdot\text{yr}^{-1}$, respectively, over the sat-
98 era (Fig. 2a, ED_Table 2a-c). By definition, one would expect (on average) ~ 4.5 5th/95th
99 percentile events per 3-month season, meaning that an increase of 0.10 $\text{d}\cdot\text{yr}^{-1}\cdot\text{yr}^{-1}$
100 accumulated over the course of the sat-era (35 years) yields an additional ~ 3.5 $\text{d}\cdot\text{yr}^{-1}$, an
101 $\sim 75\%$ increase.

102 Heatwaves, similar to those which occurred in western Russia in 2010 and Europe
103 in 2003, develop when persistent anticyclonic patterns, often referred to as “atmospheric
104 blocking”, initiate a cascade of self-reinforcing, heat-accumulating physical
105 processes^{24,25}. In addition to the increasing trends in extreme heat occurrence, robust
106 positive trends in the occurrence, persistence, and maximum duration of sat-era summer
107 mid-atmospheric anticyclonic patterns are detected over Europe (Fig. 2c, g), western Asia
108 (Fig. 3a,e), and eastern North America (ED_Fig. 4c). Robust positive trends in the
109 occurrence of sat-era anticyclonic patterns are also detected – along with increasing heat
110 extremes – in autumn over eastern North America (Fig. 3c,g), eastern Asia (Fig. 3d,h)
111 and central North America, and in spring over Europe (ED_Fig. 1).

112 Increases in hot extremes may result from dynamic changes (namely greater
113 occurrence and persistence of anticyclonic patterns), and/or from the thermodynamic
114 effects of global warming (reflected in the increased intensity of extreme temperature
115 when anticyclonic patterns occur). Over Europe, the summer occurrence of circulations
116 similar to dipole patterns with ridging over the eastern half of the domain (Fig. 2c)
117 increased 0.45 $\text{d}\cdot\text{yr}^{-1}\cdot\text{yr}^{-1}$ over the sat-era, while the persistence and maximum duration
118 increased 0.05 and 0.19 $\text{d}\cdot\text{event}^{-1}\cdot\text{yr}^{-1}$, respectively (Fig. 2g). The trend in the frequency
119 of hot events coincident with this pattern (0.06 $\text{d}\cdot\text{yr}^{-1}\cdot\text{yr}^{-1}$; Fig. 2k, ED_Table 2a)
120 accounts for 62% of the total trend in hot extremes over Europe (0.10 $\text{d}\cdot\text{yr}^{-1}\cdot\text{yr}^{-1}$; Fig. 2a).
121 In addition, the number of hot extremes per pattern occurrence has increased for all four

122 patterns (Fig. 2n-q, ED_Table 2a). Under the assumption of pattern stationarity, we
123 perform a quantitative partitioning of the dynamic and thermodynamic contributions to
124 extreme temperature trends¹⁰ (Methods). This partitioning reveals that 57% of the trend
125 in hot extremes associated with this pattern is driven by thermodynamic influences, while
126 44% is due to the dynamic influence of increased pattern occurrence (ED_Table 2a).
127 Together, these results suggest that the observed increase in extreme summer heat over
128 Europe is attributable to both increasing frequency of blocking circulations and changes
129 in the surface energy balance. Similar results are found in other regions that exhibit
130 robust upward trends in anticyclonic patterns (Fig. 3, ED_Table 2).

131 Global warming is also generally expected to decrease the frequency of cold
132 extremes¹. In autumn over eastern Asia, the occurrence of sat-era cold extremes
133 decreased $0.08 \text{ d}\cdot\text{yr}^{-1}\cdot\text{yr}^{-1}$, indicating a reduction of ~60% over the 35 year period
134 (ED_Fig. 6g and ED_Table 2f). A majority of this decreasing trend ($0.05 \text{ d}\cdot\text{yr}^{-1}\cdot\text{yr}^{-1}$;
135 ED_Table 2f) is attributable to changes associated with one pattern type: cyclonic
136 circulations capable of advecting cold air equatorward (Fig. 3d). Less frequent
137 occurrence of cyclonic patterns (Fig. 3h), in conjunction with less intense cold
138 temperature anomalies when cyclonic patterns occur (Fig. 3p), drive 63% of the overall
139 trend decrease. Of the $0.05 \text{ d}\cdot\text{yr}^{-1}\cdot\text{yr}^{-1}$ decrease in extreme cold associated with the trend
140 in cyclonic patterns, partitioning indicates 58% dynamic and 35% thermodynamic
141 contributions (ED_Table 2).

142 In contrast to this expected extreme cold decrease, winter cold extremes over
143 central Asia have increased $0.07 \text{ d}\cdot\text{yr}^{-1}\cdot\text{yr}^{-1}$ over the ice-era (ED_Fig. 7a). 150% of this
144 trend ($0.10 \text{ d}\cdot\text{yr}^{-1}\cdot\text{yr}^{-1}$; Fig. 3j) occurred when mid-atmospheric circulation was similar to
145 a pattern of troughing in the south and east, and ridging in the northwest (Fig. 3b). (Trend
146 percentages exceeding 100% indicate that other circulation patterns provide negative
147 contributions (ED_Table 2).) Occurrence and persistence of this dipole pattern robustly
148 increased ($1.0 \text{ d}\cdot\text{yr}^{-1}\cdot\text{yr}^{-1}$ and $0.12 \text{ d}\cdot\text{event}^{-1}\cdot\text{yr}^{-1}$, Fig. 3f) at the expense of all other
149 circulations (ED_Table 2d). Partitioning indicates that 75% of the extreme cold trend
150 associated with this pattern is due to the dynamic influence of increased pattern
151 occurrence, with 18% linked to thermodynamic influences (ED_Table 2d).

152 Substantial dynamic contributions to the overall trend in cold extremes could be
153 expected given that circulations that support the equatorward advection of Arctic air will
154 bring anomalously cold temperatures to lower-latitude locales²⁰. Increased occurrence of
155 such patterns has previously been observed, and linked to reduced regional sea-ice and
156 decreased baroclinicity over the Barents-Kara Seas^{4,17,26-28}. Positive thermodynamic
157 contributions to the extreme cold trend indicate processes that are in opposition to the
158 direct warming effects of enhanced radiative forcing. For example, positive
159 thermodynamic contributions from 3 of the 4 winter patterns over central Asia
160 (ED_Table 2d) suggest that these contributions are largely independent of atmospheric
161 circulation, and therefore potentially related to surface processes such as increased snow
162 cover and enhanced diabatic cooling^{4,28}.

163 The circulation trends detected here cannot as yet be attributed to anthropogenic
164 or natural causes, nor can they be projected to continue into the future. Attribution and
165 projection will require an increased understanding of the causes of the circulation trends,
166 including the ability to identify the signal of an anthropogenically forced trend from the
167 noise of internal decadal-scale climate variability^{16,29}. However, our quantitative
168 partitioning, in conjunction with targeted climate model simulations^{16,29,30}, offers the
169 potential to fingerprint dynamic and thermodynamic climate influences in isolation,
170 which in turn may facilitate attribution of the observed trends, and projection of future
171 trends. We hypothesize that the main assumption of our quantitative partitioning – pattern
172 stationarity – is justified given the expectation that circulation responses to enhanced
173 radiative forcing are likely to reinforce preexisting modes of natural variability^{15,16}. A
174 related assumption is that the reanalyses act as reasonable proxies for the state of the
175 three-dimensional atmosphere through time. Given uncertainties in the data assimilation
176 and numerical modeling that underpin atmospheric reanalysis, we have restricted our
177 identification criteria to those trends that are statistically significant in all three
178 reanalyses.

179 Our approach finds robust trends in mid-atmospheric circulation patterns over
180 some regions, and suggests that both dynamic and thermodynamic effects have
181 contributed to observed changes in temperature extremes over the past 35 years.
182 Although thermodynamic influences have largely dominated these changes, dynamic

183 influences have been critical in some regions and seasons. Long-term projections of
184 future dynamic contributions are challenging given the substantial underlying decadal-
185 scale variability, as well as the uncertain impact of anthropogenic forcing on mid-latitude
186 circulation^{15,16}. However, given our finding that many patterns have exhibited increasing
187 (decreasing) intensity of extreme hot (cold) events, and that those trends are coincident
188 with a nearly categorical increase in thermodynamic forcing, the observed trends of
189 increasing hot extremes and decreasing cold extremes could be expected to continue in
190 the coming decades, should greenhouse gases continue to accumulate in the atmosphere.

191

192 **References**

193

194 1. Field, C. B. *et al.* (eds) *Managing the Risks of Extreme Events and Disasters to*
195 *Advance Climate Change Adaptation* (Cambridge Univ. Press, 2012).

196

197 2. Donat, M. G. *et al.* Updated analyses of temperature and precipitation extreme indices
198 since the beginning of the twentieth century: The HadEX2 dataset. *J. Geophys. Res.* **118**,
199 2098–2118 (2013).

200

201 3. Francis, J. A. & Vavrus, S. J. Evidence linking Arctic amplification to extreme weather
202 in mid-latitudes. *Geophys. Res. Lett.* **39**, L06801 (2012).

203

204 4. Liu, J., Curry, J. A., Wang, H., Song, M. & Horton, R. M. Impact of declining Arctic
205 sea ice on winter snowfall. *Proc. Natl Acad. Sci. USA* **109**, 4074–4079 (2012).

206

207 5. Petoukhov, V., Rahmstorf, S., Petri, S. & Schellnhuber, H. J. Quasiresonant
208 amplification of planetary waves and recent Northern Hemisphere weather extremes.
209 *Proc. Natl Acad. Sci. USA* **110**, 5336–5341 (2013).

210

211 6. Screen, J. A. & Simmonds, I. Caution needed when linking weather extremes to
212 amplified planetary waves. *Proc. Natl Acad. Sci. USA* **110**, E2327 (2013).

213

- 214 7. Barnes, E. A., Dunn-Sigouin, E., Masato, G. & Woolings, T. Exploring recent trends in
215 Northern Hemisphere blocking. *Geophys. Res. Lett.* **41**, 638-644 (2014).
216
- 217 8. Screen, J. & Simmonds, I. Exploring links between Arctic amplification and mid-
218 latitude weather. *Geophys. Res. Lett.* **40**, 959-964 (2013).
219
- 220 9. Kohonen, T. *Self-Organizing Maps* p. 501, (Springer, 2001)
221
- 222 10. Cassano, J. J., Uotila, P., Lynch, A. H. & Cassano, E. N. Predicted changes in
223 synoptic forcing of net precipitation in large Arctic river basins during the 21st century. *J.*
224 *Geophys. Res.* **112**, G04S49 (2007).
225
- 226 11. Johnson, N. C., Feldstein, S. B. & Tremblay, B. The continuum of Northern
227 Hemisphere teleconnection patterns and a description of the NAO shift with the use of
228 self-organizing maps. *J. Climate* **21**, 6354-6371 (2008).
229
- 230 12. Lee, S. & Feldstein, S. B. Detecting ozone- and greenhouse gas-driven wind trends
231 with observational data. *Science* **339**, 563-567 (2013).
232
- 233 13. Diffenbaugh, N. S. *et al.* in *Climate Change 2014: Impacts, Adaptation, and*
234 *Vulnerability* (eds. Field, C. B. *et al.*) 137-141 (IPCC, Cambridge Univ. Press, 2014).
235
- 236 14. Field C. B. *et al.* in *Climate Change 2014: Impacts, Adaptation, and Vulnerability*
237 (eds. Field, C. B. *et al.*) 1-32 (IPCC, Cambridge Univ. Press, 2014).
238
- 239 15. Shepherd, T. G. Atmospheric circulation as a source of uncertainty in climate change
240 projections. *Nature Geosci.* **7**, 703-708 (2014).
241
- 242 16. Deser, C., Phillips, A. S., Alexander, M. A. & Smoliak, B. V. Projecting North
243 American climate over the next 50 years: uncertainty due to internal variability. *J.*
244 *Clim.* **27**, 2271–2296 (2014).

245

246 17. Cohen J. *et al.* Recent Arctic amplification and extreme mid-latitude weather. *Nature*
247 *Geosci.* **7**, 627-637 (2014).

248

249 18. Palmer, T. Record-breaking winters and global climate change. *Science* **344**, 803–804
250 (2014).

251

252 19. Wallace, J. M., Held, I. M., Thompson, D. W. J., Trenberth, K. E. & Walsh, J. E.
253 Global warming and winter weather. *Science* **343**, 729–730 (2014).

254

255 20. Screen, J. A. Arctic amplification decreases temperature variance in northern mid- to
256 high-latitudes. *Nature Clim. Change* **4**, 577-582 (2014).

257

258 21. Hartmann, D. L. *et al.* in *Climate Change 2013: The Physical Science Basis* (eds.
259 Stocker, T. F. *et al.*) 159-254 (IPCC, Cambridge Univ. Press, 2013).

260

261 22. Simmonds, I. Comparing and contrasting the behaviour of Arctic and Antarctic sea
262 ice over the 35-year period 1979-2013. *Ann. Glaciol.* **56**, 18-28 (2015).

263

264 23. Diffenbaugh N.S. & Ashfaq, M. Intensification of hot extremes in the United States.
265 *Geophys. Res. Lett.* **37**, L15701 (2010).

266

267 24. Miralles, D. G., Teuling, A. J., van Heerwaarden, C. C. & Vila-Guerau de Arellano, J.
268 Mega-heatwave temperatures due to combined soil desiccation and atmospheric heat
269 accumulation. *Nature Geosci.* **7**, 345-349 (2014).

270

271 25. Diffenbaugh, N. S., Pal, J. S., Trapp, R. J. & Giorgi, F. Fine-scale processes regulate
272 the response of extreme events to global climate change. *Proc. Natl Acad. Sci. USA* **102**,
273 15774-15778 (2005).

274

- 275 26. Inoue, J., Hori, M. E. & Takaya, K. The role of Barents Sea ice in wintertime cyclone
276 tracks emergence of a warm-Artic cold-Siberian Anomaly. *J. Climate* **25**, 2561-2568
277 (2012).
278
- 279 27. Mori, M., Watanabe, M., Shiogama, H., Inoue, J. & Kimoto, M. Robust Arctic sea-ice
280 influence of the frequent Eurasian cold winters in past decades. *Nature Geosci.* **7**, 869-
281 873 (2014).
282
- 283 28. Cohen, J., Furtado, J., Barlow, J. M., Alexeev, V. & Cherry, J. Arctic warming,
284 increasing fall snow cover and widespread boreal winter cooling. *Environ. Res. Lett.* **7**,
285 014007 (2012).
286
- 287 29. Screen, J.A., Deser, C., Simmonds, I. & Tomas, R. Atmospheric impacts of Arctic
288 sea-ice loss, 1979-2009: Separating forced change from atmospheric internal variability.
289 *Climate Dyn.* **43**, 333-344 (2014).
290
- 291 30. Screen, J.A., Simmonds, I., Deser, C. & Tomas, R. The atmospheric response to three
292 decades of observed Arctic sea ice loss. *J. Climate* **26**, 1230-1248 (2013).
293

294 **Acknowledgements**

295 Work by D.E.H., D.S., D.L.S., and N.S.D. was supported by NSF CAREER
296 Award 0955283, DOE Integrated Assessment Research Program Grant No. DE-
297 SC005171DE-SC005171, and a G.J. Lieberman Fellowship to D.S. Contributions from
298 N.C.J. were supported by NOAA's Climate Program Office's Modeling, Analysis,
299 Predictions, and Projections program award #NA14OAR4310189. B.R. acknowledges
300 support from the US Air Force Office of Scientific Research (FA9550-13-1-0043), the
301 US National Science Foundation (DMS-0906392, DMS-CMG-1025465, AGS-1003823,
302 DMS-1106642, and DMS-CAREER-1352656), the Defense Advanced Research Projects
303 Agency (DARPA YFA N66001-111-4131), and the UPS Foundation (SMC-DBNKY).
304 We thank J. Cattiaux, D. Touma, and J.S. Mankin for discussions that improved the
305 manuscript. Computational resources for data processing and analysis were provided by

306 the Center for Computational Earth and Environmental Science in the School of Earth,
307 Energy, and Environmental Sciences at Stanford University.

308

309 **Author Contributions**

310 D.E.H. conceived the study. D.E.H., N.C.J., D.S., D.L.S., and N.S.D. designed the
311 analysis and co-wrote the manuscript. D.E.H., N.C.J., and D.S. provided analysis tools.
312 D.E.H. performed the analysis. B.R. provided and described the multiple hypothesis
313 testing and transformation analysis.

314

315 **Competing Financial Interests**

316 The Authors declare no competing financial interests.

317

318 **Corresponding Author**

319 Daniel E. Horton, danethan@stanford.edu

320

321 **Figure & Table Legends**

322

323 **Table 1 | Trends in surface temperature extremes and atmospheric circulation**
324 **patterns.** Trends are calculated for each NH season (DJF-winter, MAM-spring, JJA-
325 summer, SON-autumn) for two periods, 1979-2013 (sat-era) and 1990-2013 (ice-era).
326 Regional domains (see Fig. 2a) in which one or more of the four SOM circulation
327 patterns demonstrate robust trends in mid-atmospheric circulation pattern occurrence (O),
328 persistence (P), or maximum duration (M) are shown in green (ED_Figs 1-2). Positive
329 (+) and negative (-) symbols are displayed when all three reanalyses show statistically
330 significant trends in a particular circulation pattern, and agree on the sign of those trends.
331 Multiple symbols within a box indicate multiple robust pattern trends. White boxes
332 without symbols indicate no statistically significant trends and/or reanalysis disagreement
333 (see Methods). Regional domains with positive and/or negative trends in cold (05) and/or
334 hot (95) extremes receive (+) or (-) symbols when the three reanalyses agree on the sign
335 of the area-weighted trend. Red and blue boxes indicate that the extreme temperature

336 trend results in warming and cooling, respectively, while gray boxes indicate reanalysis
337 disagreement.

338

339 **Figure 1 | Trends in mid-atmospheric geopotential height anomalies.** Northern
340 Hemisphere polar projections of 1979-2013 seasonal trends [$\text{m}\cdot\text{yr}^{-1}$] in 500 hPa
341 geopotential height anomalies. The time-series of seasonal mean anomalies is calculated
342 from the daily anomalies generated by subtracting the seasonal cycle from each grid cell.
343 Trends are computed for **a**, winter (DJF), **b**, spring (MAM), **c**, summer (JJA), and **d**,
344 autumn (SON) seasons. Geopotential height fields are sourced from NCEP-DOE-R2.

345

346 **Figure 2 | Trends in circulation patterns and hot extremes over Europe.** **a**, 1979-
347 2013 trends in summer hot extreme occurrences for all regional domains based on 2-
348 meter maximum/minimum temperatures from NCEP-DOE-R2. **b-e**, SOM-derived mid-
349 atmospheric circulation patterns (500 hPa geopotential height anomalies) over Europe.
350 White-boxed values show pattern frequencies (%) in the top left, and SOM node numbers
351 in the top right. **f-i**, Time-series of SOM circulation pattern occurrence (black; [$\text{d}\cdot\text{yr}^{-1}$]),
352 persistence (blue; [$\text{d}\cdot\text{event}^{-1}$]), and maximum duration (red; [$\text{d}\cdot\text{event}^{-1}$]). The slope of the
353 trend line [yr^{-1}] and p-values (in parentheses) are color coded, with the values from 1979-
354 2013 (solid trend line) displayed above those from 1990-2013 (dashed trend line). **j-m**,
355 Spatially rendered trends in hot extreme occurrences for days that correspond to each
356 SOM circulation pattern. **n-q**, Time-series of the area-weighted mean of hot extremes per
357 pattern occurrence, referred to throughout the text as a measure of the intensity of
358 temperature extremes associated with each pattern. Statistically significant trends (5%
359 significance level) are shown by stippling in the mapped panels and by bold fonts in the
360 scatter plots.

361

362 **Figure 3 | Circulation pattern and thermal extreme trends for selected regions.**
363 Trends in thermal extreme occurrences for selected regions and seasons based on 2-meter
364 maximum/minimum temperatures from NCEP-DOE-R2. **a-d**, SOM-derived mid-
365 atmospheric circulation patterns (500 hPa geopotential height anomalies) over western
366 Asia in summer (**a**), central Asia in winter (**b**), eastern North America in autumn (**c**), and

367 eastern Asia in autumn (**d**). White-boxed values show pattern frequencies (%) in the top
368 left, and SOM node numbers in the top right. In contrast to Fig. 2, just one of the four
369 SOM circulation patterns is displayed from each region. **e-h**, Time-series of SOM
370 circulation pattern occurrence (black; [$\text{d}\cdot\text{yr}^{-1}$]), persistence (blue; [$\text{d}\cdot\text{event}^{-1}$]), and
371 maximum duration (red; [$\text{d}\cdot\text{event}^{-1}$]). The slope of the trend line [yr^{-1}] and p-values (in
372 parentheses) are color coded, with the values from 1979-2013 (solid trend line) displayed
373 above those from 1990-2013 (dashed trend line). **i-l**, Spatially rendered trends in thermal
374 extreme occurrences for days that correspond to each SOM circulation pattern. **m-p**,
375 Time-series of the area-weighted mean of temperature extremes per pattern occurrence,
376 referred to throughout the text as a measure of the intensity of temperature extremes
377 associated with each pattern. Statistically significant trends (5% significance level) are
378 shown by stippling in the mapped panels and by bold fonts in the scatter plots. Refer to
379 Extended Data Figs. 6 and 7 for sat-era and ice-era trends in temperature extremes over
380 the regional domains.

381

382 **Methods**

383 *Categorization of Circulation Patterns*

384 We use SOM cluster analysis⁹⁻¹² to categorize large-scale circulation patterns over
385 seven Northern Hemisphere domains³¹ using daily 500 hPa geopotential height anomaly
386 fields from the NCAR/NCEP-R1 (32), NCEP-DOE-R2 (33), and ECMWF ERA-Interim
387 (34) reanalyses. Daily anomalies are calculated by subtracting the seasonal cycle
388 (calendar-day mean) from each grid cell. Reanalyses are analyzed individually to
389 maintain their physical consistency, and to facilitate their intercomparison. The SOMs'
390 unsupervised learning algorithm requires neither *a priori* knowledge of which types of
391 circulation patterns might be detected, nor the specific geographic regions in which they
392 might occur. Geopotential height anomaly fields from each day are assigned to one of a
393 pre-defined number of nodes, according to pattern similarity. The final SOM patterns are
394 obtained by minimizing the Euclidian distance between iteratively updated nodes and
395 their matching daily geopotential height anomaly fields¹¹. Each SOM pattern can
396 therefore be viewed as a representative composite of relatively similar circulation
397 patterns.

398 Due to global-scale warming, trends in geopotential height anomalies record both
399 altered atmospheric circulation patterns and the thermal expansion of the troposphere. To
400 isolate the signal of circulation pattern change, previous clustering analyses have
401 assumed uniform thermal dilation and removed either the domain average³⁵ or domain
402 average linear trend³⁶ from the daily-scale anomalies. In our analysis, we find that 1979-
403 2013 trends in Northern Hemisphere geopotential height anomalies are non-uniform in
404 both magnitude and sign (Fig. 1), and demonstrate substantial seasonal, regional, and
405 latitudinal differences (ED_Fig. 3e). These findings suggest that for the relatively short
406 period of our analysis, an assumption of uniform thermal dilation is inappropriate.
407 Moreover, the strong spatial heterogeneity indicates the importance of large-scale
408 dynamics in the regional geopotential height trends, and so the removal of local
409 geopotential height trends would conflate dynamic changes with thermal dilation.
410 Therefore, in the main text we present results and conclusions based on raw geopotential
411 height data. However, despite the lack of uniform expansion, we have conducted an
412 analysis that attempts to account for the effects of thermal dilation. SOM analyses are
413 performed on geopotential heights that have been detrended by removing the seasonal
414 mean hemispheric trend (ED_Fig. 3e) from each grid cell. Results from this analysis
415 indicate that the magnitude, significance, and sign of circulation trends are sensitive to
416 the method of controlling for thermal expansion (ED_Fig. 3f-j). Despite this sensitivity,
417 the conclusions presented in the main text are supported, in that both raw and detrended
418 analyses generally suggest trends of similar magnitude, sign, and significance.

419 Based on domain-wide pattern correlations between daily height field anomalies
420 and different SOM node counts¹² (ED_Fig. 8), we divide circulation patterns over each
421 domain into four SOM nodes (e.g., Fig. 2b-e). To determine a suitable number of nodes,
422 a suite of different node counts were analyzed. We found that four nodes were
423 sufficiently great in number to capture a diversity of highly generalized circulation
424 patterns, but sufficiently few to facilitate convenient presentation and – critically – to
425 prevent overly similar SOM patterns¹². To test the sensitivity of our results to the number
426 of nodes, we present 2-, 4-, 8-, and 16-node SOMs for the summer season over the
427 European domain (ED_Figs. 1-2). Based on these analyses, it is apparent that a 2-node
428 SOM is insufficient to capture the diversity of circulation patterns that are found in the

429 reanalysis data (ED_Fig. 1a), whereas 8- and 16-node SOMs produce nodes with overly
430 similar circulation patterns (ED_Figs. 1c and 2). Examination of the 4-, 8-, and 16-node
431 SOMs largely verifies the conclusions drawn from the 4-node SOM: that the occurrence
432 of patterns with ridging over the eastern half of the domain has increased over time, while
433 the occurrence of complimentary patterns has decreased. We note that these pattern
434 trends are not identified in the 2-node SOM, confirming that two nodes are too few to
435 capture specific circulation patterns that are critical for extreme temperature occurrence.
436 Similar node-count analyses for other regions/seasons likewise verify the conclusions
437 drawn from the 4-node analyses that are presented in the main text (not shown).

438

439 *Calculation of Robust Trends In Circulation Patterns*

440 For each season in each year, we calculate (1) the total number of days on which
441 each SOM pattern occurs (“occurrence”; [d•yr⁻¹]), (2) the mean length of consecutive
442 occurrence (“persistence”; [d•event⁻¹]), and (3) the longest consecutive
443 occurrence (“maximum duration”; [d•event⁻¹]). A trend in one of these characteristics is
444 considered robust when the trend in that pattern is (1) statistically significant in all three
445 reanalyses, and (2) of the same sign in all three reanalyses. Trends with
446 regression coefficients that surpass the 5% significance (95% confidence) threshold are
447 considered statistically significant. Trends are calculated across sat-era and ice-era annual
448 time-series using the approach of Zwiers and von Storch (37), which allows us to account
449 for temporal dependence. Here the trends are calculated using linear least squares
450 regression, but to account for temporal dependence, the confidence bounds of annual
451 time-series trends with lag-1 autocorrelation greater than the 5% significance level are
452 recalculated by adjusting the number of degrees of freedom used to compute the
453 regression coefficient significance³⁷. As a result, unlike a simple linear regression, this
454 approach does not rely on the independent and identically distributed (“i.i.d.”)
455 assumption for the residuals, but instead accounts for temporal dependence using a red
456 noise assumption.

457 The approach of ref. 37 also assumes that the distribution of the residuals is
458 Gaussian. Using the Anderson-Darling³⁸ test for normality, we find that 91-100% of
459 residual distributions in each metric of each reanalysis do not reject the null hypothesis of

460 Gaussianity when multiple hypothesis testing controlling the Familywise Error Rate³⁹
461 (FWER) at the 5% significance level is considered (ED_Table 1b). The Gaussianity
462 assumption is therefore largely appropriate. However, due to the identification of non-
463 normality in some distributions, particularly in the persistence and maximum duration
464 metrics, we apply Box-Cox power transformations⁴⁰ to all distributions. Using the
465 Anderson-Darling test, we find that 96-100% of the distributions of the residuals in the
466 transformed setting do not reject the null hypothesis of Gaussianity at the 5% significance
467 level. Further, when multiple hypothesis testing is considered by controlling the FWER at
468 the 5% level, 100% of the individual tests are non-significant (ED_Table 1b). In addition,
469 the number of pattern trends identified as significant in the transformed case is largely
470 consistent with the non-transformed regression analysis. However, additional significant
471 trends in the persistence and maximum duration metrics are identified when Box-Cox
472 transformations are used (ED_Table 1a). The large overlap of results between the
473 transformed and non-transformed analyses suggests that although individual residual
474 distributions may vary, the Gaussian assumption applied throughout this study is for the
475 most part quite robust, though in some cases not valid. In sum, the non-transformed
476 analysis that fits a linear relationship to circulation pattern metrics allows for a relatively
477 simple classification of two short analysis periods, while simultaneously accounting for
478 temporal dependence in a large number (>2000) of individual time-series (7 regions \times 4
479 nodes \times 4 seasons \times 3 characteristics \times 2 time periods \times 3 reanalyses).

480 Because SOM nodes are calculated independently for each reanalysis, individual
481 SOM patterns must be matched between the three reanalyses in order to determine
482 whether an individual pattern shows robust results across all three reanalyses. To
483 determine which SOM patterns are the closest match between the three reanalyses, the
484 root mean square error (RMSE) is calculated between the SOM patterns of one reanalysis
485 and those of the other reanalyses. Patterns with the smallest RMSEs are considered
486 matches. Although we undertake a multi-reanalysis robustness evaluation, further work is
487 needed to confirm that other available reanalyses (such as CFSR and MERRA) show the
488 same trends.

489

490 *Multiple Hypothesis Testing of Linear Trends*

491 It is possible that some of the trends identified as significant in any individual
492 reanalysis could occur by chance. In addition to screening for those patterns that are
493 significant in all three reanalyses (our “robustness” criterion), we also employ formal
494 multi-hypothesis testing utilizing several methodologies. The first is the familywise error
495 rate (FWER). This type of error metric controls the probability of falsely rejecting any
496 null hypothesis, and is considered one of the strictest forms of error control³⁹. Since a
497 certain number of false rejections can happen by chance alone, one can account for this
498 formally by using the k-FWER or k-familywise error rate⁴¹ (k-FWER). The k-FWER
499 controls the probability of falsely rejecting k or more null hypotheses, and aims to
500 formalize the concept that some of the hypotheses will be rejected by chance. One option
501 for the value of k is to use the expected number of hypotheses that will be rejected at a
502 given significance level. For instance, in our study, out of 112 total “local” hypotheses, 5
503 or 6 hypothesis will be significant at the 5% significance level by chance ($112 \times 0.05 =$
504 5.6). In this case, one can evaluate the probability that 7 or more hypothesis are falsely
505 rejected, since on average about 6 could be rejected as significant by chance. The third
506 metric is the false discovery rate (FDR), which controls the expectation of the ratio given
507 by the number of false rejections divided by the total number of rejections³⁹.

508 All of the above measures of error control aim to guard against hypotheses being
509 falsely declared as significant in the context of multiple tests. To be thorough, we have
510 implemented all three types of error control at both global significance levels of 5% and
511 10%. The results of these analyses are summarized in Extended Data Table 2. We note
512 that all three metrics heavily favor the null as they are designed to protect against the
513 possibility of false positives. Despite this, the presence of local tests that reject the null
514 represents a strong confirmation of the significance of those local tests. The fact that a
515 number of local hypotheses still prevail as significant, even after imposing much stricter
516 multiple testing error controls, arises partly from the fact that some of the local p-values
517 indicate trends that are so highly significant that they can withstand the stricter multiple
518 testing error control metrics. We believe that this rigorous multiple-testing error control
519 yields increased credibility to the scientific conclusions of robust trends in pattern
520 occurrence.

521

522 ***Temperature Extremes***

523 Daily-scale hot and cold extreme occurrences are calculated using temperature
524 anomalies at each grid cell. Temperature anomalies are computed by removing the
525 seasonal cycle from daily reanalysis 2-meter maximum/minimum temperatures. Similar
526 to previous studies^{1,2}, temperature extremes are calculated based on the statistical
527 distribution of daily temperature anomalies²⁰. Hot/cold extreme thresholds are defined as
528 the 95th/5th percentile value of the 1979–2013 daily 2-meter maximum/minimum
529 temperature anomaly distribution (e.g., for JJA, the population of daily-maximum
530 temperature anomalies from the months of June, July and August in the years 1979-
531 2013). Hot/cold extreme occurrences are defined as days on which the daily temperature
532 anomalies are greater/less than (or equal to) the hot/cold extreme thresholds. Reanalysis
533 temperature extremes are qualitatively similar to those found in station-based
534 observations². Given this similarity, we use the reanalysis temperatures in order to
535 maintain internal physical consistency between daily 2-meter temperatures and daily
536 atmospheric circulation (as represented by the 500 hPa SOM circulation patterns). Trends
537 in temperature extreme occurrence are computed across sat-era and ice-era annual time-
538 series following the methodology of ref. 37.

539

540 ***Quantitative Partitioning***

541 To determine the dynamic and thermodynamic contributions to trends in
542 temperature extreme occurrence, we adapt the climate change partitioning methodology
543 of Cassano *et al* (10). Our adapted methodology partitions the contributions of dynamic
544 and thermodynamic changes to (1) the overall trend in temperature extreme occurrence
545 and (2) the trends associated with individual SOM circulation patterns. Previous
546 applications of the Cassano *et al* methodology indicate that partitioning is largely
547 insensitive to the number of SOM nodes used in the analysis⁴². All trends in temperature
548 extremes in the below methodology are area-weighted averages. Following Cassano *et al*:

$$E = \sum_{i=1}^K E_i f_i$$

549 where E is the frequency of extreme temperature occurrence, f_i is the frequency of
550 occurrence of SOM pattern i , E_i is the frequency of extreme temperature occurrence

551 when SOM pattern i occurs, and K is the total number of SOM nodes. We decompose E
 552 and f into time mean and deviation from time mean components:

$$E = \sum_{i=1}^K (\bar{E}_i + E_i')(\bar{f}_i + f_i')$$

553 Now we differentiate the above equation with respect to time, noting that the mean values
 554 are constants:

$$\frac{dE}{dt} = \sum_{i=1}^K (\bar{f}_i \frac{dE_i'}{dt} + \bar{E}_i \frac{df_i'}{dt} + \frac{d}{dt}(E_i' f_i'))$$

555 The derivative on the left-hand side provides the area-weighted average trend in
 556 the seasonal occurrence of temperature extremes for all days. The summation on the
 557 right-hand side, from left to right, provides the thermodynamic, dynamic, and interaction
 558 contributions for days associated with each SOM pattern, i .

559 The thermodynamic contribution of each circulation pattern's extreme
 560 temperature trend assumes that each SOM pattern is stationary in time, and that trends in
 561 extremes that result during this pattern are the result of influences unrelated to
 562 circulation, such as changes in longwave radiation from increasing greenhouse gas
 563 concentrations, or changes in surface fluxes of moisture and/or radiation resulting from
 564 changes in land cover. The thermodynamic contribution associated with each circulation
 565 pattern is determined by taking the product of the trend in the intensity of temperature
 566 extremes and the mean occurrence of the circulation pattern. Trends in the intensity of
 567 temperature extremes are computed by calculating the trend in area-weighted extreme
 568 occurrence per pattern occurrence (e.g., Fig. 2n-q).

569 The dynamic contribution of each circulation pattern's extreme temperature trend
 570 assumes that, on average, a circulation pattern is associated with a portion of the total
 571 extreme event trend, and that changes in the occurrence frequency of that circulation
 572 pattern will modify the occurrence frequency of extreme events. The dynamic
 573 contribution associated with each circulation pattern is determined by taking the product
 574 of the trend in circulation pattern occurrences and the mean number of extreme events per
 575 pattern occurrence.

576 The third component represents the interaction between dynamic and
 577 thermodynamic changes, and captures contributions that result from changes in the

578 dynamic component acting on changes in the thermodynamic component, such as the
579 positive/negative feedbacks of surface-atmosphere interactions. The interactive term is
580 determined by computing the trend in the product of circulation pattern occurrence
581 deviations and intensity of temperature extreme deviations.

582

583 ***Code Availability***

584 SOM code is available at: <http://www.cis.hut.fi/projects/somtoolbox/>. All other
585 analysis code is available upon request from the corresponding author via email:
586 danethan@stanford.edu.

587

588 **Method References**

589

590 31. Screen, J. A. & Simmonds, I. Amplified mid-latitude planetary waves favour
591 particular regional weather extremes. *Nature Clim. Change* **4**, 704-709 (2014).

592

593 32. Kalnay, E., *et al.* The NCEP/NCAR 40-year reanalysis project, *Bull. Am. Meteorol.*
594 *Soc.*, **83**, 437–471 (1996).

595

596 33. M. Kanamitsu, W. *et al.* NCEP-DOE AMIP-II Reanalysis (R-2). *Bull. Am. Meteorol.*
597 *Soc.* **83**, 1631-1643 (2002).

598

599 34. Dee, D. P. *et al.* The ERA-Interim reanalysis: configuration and performance of the
600 data assimilation system. *Q. J. R. Meteorol. Soc.* **137**, 553–597 (2011).

601

602 35. Driouech, F., Déqué M. & Sánchez-Gómez, E. Weather-regimes-Moroccan
603 precipitation link in a regional climate change simulation. *Glob. Plan. Ch.* **72**, 1-10
604 (2010).

605

606 36. Cattiaux, J., Douville, H. & Peings, P. European temperatures in CMIP5: origins of
607 present-day biases and future uncertainties. *Clim. Dyn.* **41** 2889-2907 (2013).

608

609 37. Zwiers, F. W. & von Storch, H. Taking serial correlation into account in tests of the
610 mean. *J. Clim.* **8**, 336-351 (1995).

611

612 38. Anderon, T.W. & Darling, D.A. Asymptotic theory of certain “goodness-of-fit”
613 criteria based on stochastic processes. *Ann. Math. Statist.* **23**, 193-212 (1952).

614

615 39. Benjamini, Y. & Hochberg, Y. Controlling the false discovery rate: A practical and
616 powerful approach to multiple testing. *J. Roy. Statist. Soc. Ser. B* **57**, 289-300 (1995).

617

618 40. Box, G.E.P. & Cox, D.R. An analysis of transformations. *J. Roy. Statist. Soc. Ser. B*
619 **26**, 211-243 (1964).

620

621 41. Lehmann, E. & Romano, J. P. Generalizations of the familywise error rate. *The*
622 *Annals of Statistics* **33**, 1138–1154 (2005).

623

624 42. Skific, N., Francis, J. A. & Cassano, J. J. Attribution of projected changes in
625 atmospheric moisture transport in the Arctic: A self-organizing map perspective. *J. Clim.*
626 **22**, 4135-4153 (2009).

627

628 **Data**

629 ***Reanalysis Datasets***

630 NCAR/NCEP-Reanalysis 1 data downloaded from: www.esrl.noaa.gov/psd/

631 NCEP-DOE-Reanalysis 2 data downloaded from: www.esrl.noaa.gov/psd/

632 ECMWF ERA-Interim data downloaded from: www.ecmwf.int/

633

634 **Extended Data Figure & Table Legends:**

635

636 **Extended Data Figure 1 | 2-, 4-, and 8-node SOM analyses.** SOM-derived mid-
637 atmospheric summer (JJA) circulation patterns (500 hPa geopotential height anomalies)
638 over Europe using **a**, 2-, **b**, 4-, and **c**, 8-node analyses. White-boxed values show pattern
639 frequencies (%) in the top left, and SOM node numbers in the top right. Time-series of

640 SOM circulation pattern occurrence (black; [$d \cdot yr^{-1}$]), persistence (blue; [$d \cdot event^{-1}$]), and
641 maximum duration (red; [$d \cdot event^{-1}$]). The slope of the trend line [yr^{-1}] and p-values (in
642 parentheses) are color coded, with the values from 1979-2013 (solid trend line) displayed
643 above those from 1990-2013 (dashed trend line). Statistically significant trends (5%
644 significance level) are shown by bold fonts in the scatter plots. Geopotential height fields
645 are sourced from the NCEP-DOE-R2 reanalysis³³.

646

647 **Extended Data Figure 2 | 16-node SOM analysis.** SOM-derived mid-atmospheric
648 summer (JJA) circulation patterns (500 hPa geopotential height anomalies) over Europe
649 derived from a 16-node analysis. White-boxed values show pattern frequencies (%) in the
650 top left, and SOM node numbers in the top right. Time-series of SOM circulation pattern
651 occurrence (black; [$d \cdot yr^{-1}$]), persistence (blue; [$d \cdot event^{-1}$]), and maximum duration (red;
652 [$d \cdot event^{-1}$]). The slope of the trend line [yr^{-1}] and p-values (in parentheses) are color
653 coded, with the values from 1979-2013 (solid trend line) displayed above those from
654 1990-2013 (dashed trend line). Statistically significant trends (5% significance level) are
655 shown by bold fonts in the scatter plots. Geopotential height fields are sourced from the
656 NCEP-DOE-R2 reanalysis³³.

657

658 **Extended Data Figure 3 | Geopotential height anomaly trends and thermal dilation**
659 **adjustment. a-d,** Northern Hemisphere polar projections of 1979-2013 seasonal trends in
660 500 hPa geopotential height anomalies (same as Fig.1, reproduced here for convenience).
661 **e,** Area-weighted trends in seasonal geopotential height anomalies over the Northern
662 Hemisphere and regional SOM domains. **f-j,** Trends in raw and detrended geopotential
663 height SOM pattern occurrence (OCC), persistence (PER), and maximum duration
664 (DUR) in units of $d \cdot yr^{-2}$ for domains and seasons highlighted in the main text. The
665 magnitudes of the (removed) seasonal Northern Hemisphere trends can be found in **e**.
666 Grid cells highlighted in gray contain trends significant at the 5% level. SOM circulation
667 patterns are abbreviated by letter: A-Anticyclonic, C-Cyclonic, and combinations of the
668 two represent dipole patterns and east-west configurations. Geopotential height fields are
669 sourced from the NCEP-DOE-R2 reanalysis³³.

670

671 **Extended Data Figure 4 | 1979-2013 (sat-era) robust atmospheric circulation pattern**
672 **trends.** Time-series of circulation pattern occurrence (black; [$d \cdot yr^{-1}$]), persistence (blue;
673 [$d \cdot event^{-1}$]), and maximum duration (red; [$d \cdot event^{-1}$]) from the NCEP-DOE-R2
674 reanalysis³³: **a**, summer over Europe; **b**, summer over western Asia; **c**, summer over
675 eastern North America; **d**, autumn over eastern Asia; **e**, autumn over western Asia; **f**,
676 autumn over central North America; **g**, autumn over eastern North America; and **h**, spring
677 over Europe. Statistically significant trends ($[yr^{-1}]$; 5% significance level) are identified
678 by bold fonts in the scatter plots.

679

680 **Extended Data Figure 5 | 1990-2013 (ice-era) robust atmospheric circulation pattern**
681 **trends.** Time-series of circulation pattern occurrence (black; [$d \cdot yr^{-1}$]), persistence (blue;
682 [$d \cdot event^{-1}$]), and maximum duration (red; [$d \cdot event^{-1}$]) from the NCEP-DOE-R2
683 reanalysis³³: **a**, winter over western Asia; **b**, winter over central Asia; **c**, summer over
684 western Asia; **d**, summer over eastern North America; **e**, autumn over western Asia; and
685 **f**, autumn over eastern North America. Statistically significant trends ($[yr^{-1}]$; 5%
686 significance level) are identified by bold fonts in the scatter plots.

687

688 **Extended Data Figure 6 | 1979-2013 (sat-era) Northern Hemisphere extreme**
689 **temperature occurrence trends.** Sat-era extreme temperature trends [$d \cdot yr^{-1} \cdot yr^{-1}$] for
690 winter cold (**a**) and hot (**b**) occurrences; spring cold (**c**) and hot (**d**) occurrences; summer
691 cold (**e**) and hot (**f**) occurrences; and autumn cold (**g**) and hot (**h**) occurrences. Trends are
692 calculated from the NCEP-DOE-R2 reanalysis 2-meter daily maximum/minimum
693 temperatures³³. Grid cells with statistically significant trends (5% significance level) are
694 stippled.

695

696 **Extended Data Figure 7 | 1990-2013 (ice-era) Northern Hemisphere extreme**
697 **temperature occurrence trends.** Ice-era extreme temperature trends [$d \cdot yr^{-1} \cdot yr^{-1}$] for
698 winter cold (**a**) and hot (**b**) occurrences; spring cold (**c**) and hot (**d**) occurrences; summer
699 cold (**e**) and hot (**f**) occurrences; and autumn cold (**g**) and hot (**h**) occurrences. Trends are
700 calculated from the NCEP-DOE-R2 reanalysis 2-meter daily maximum/minimum

701 temperatures³³. Grid cells with statistically significant trends (5% significance level) are
702 stippled.

703

704 **Extended Data Figure 8 | Sensitivity of pattern similarity to number of SOM nodes.**

705 To determine an adequate number of SOM nodes, we follow a modified version of the
706 methodology introduced by Lee and Feldstein (12), wherein the mean pattern correlation
707 of all daily geopotential height anomaly fields and their matching SOM node patterns are
708 computed for a suite of different SOM node counts (3, 4, 5, 6, 7, and 8), for all regions
709 and all seasons (black dots). We also compute the maximum/minimum pattern correlation
710 of daily geopotential height anomaly fields with their matching SOM node pattern (red
711 dots) and the maximum/minimum SOM-pattern-to-SOM-pattern correlation (blue
712 triangles). The goal is to select an adequate number of nodes such that: (1) the mean
713 pattern correlation of all daily geopotential height anomaly fields is relatively large, (2)
714 the minimum pattern correlation of daily geopotential height anomaly fields is relatively
715 large, and (3) the maximum SOM-pattern-to-SOM-pattern correlation is relatively small.
716 Similar to Lee and Feldstein, we find that four SOM nodes are generally sufficient to
717 capture the different modes of atmospheric variability, but small enough that SOM
718 patterns depict distinct circulations. Geopotential height anomaly fields are sourced from
719 the NCEP-DOE-R2 reanalysis³³.

720

721 **Extended Data Table 1 | Significant reanalysis circulation pattern trends and
722 summary of multiple hypothesis testing. a,** Here we indicate the number of linear

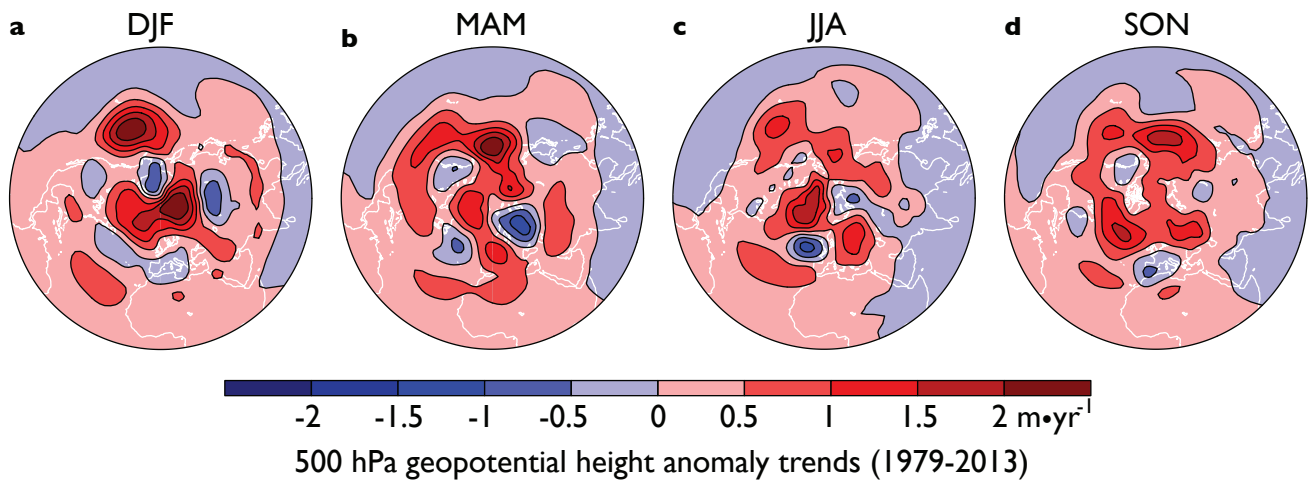
723 regression and Box-Cox transformed statistically significant occurrence (occ), persistence
724 (per), and maximum duration (max dur) trends that surpass the 95% confidence threshold
725 (5% significance level) for each reanalysis in each analysis period (1979-2013 = “sat-era”
726 and 1990-2013 = “ice-era”). For a given metric (occ, per and max dur) in a given period
727 (sat-era and ice-era), there are four patterns per region, over four seasons, for 7 domains.
728 There are therefore 112 total trends in each metric in each period. **b,** Results of
729 Anderson-Darling³⁸ (AD) tests of normality indicating the number of original and Box-
730 Cox transformed⁴⁰ distributions of residuals that do not reject the null hypothesis of
731 Gaussianity at the 5% level. For both the original and Box-Cox AD tests, we also apply

732 multiple hypothesis testing to control the Familywise Error Rate³⁹ (FWER) at the 5%
733 significance level. **c**, To protect against the possibility of false positives in the linear
734 regression trend analyses, for each reanalysis, we use three different multiple hypothesis
735 error control methodologies to assess the number of locally significant hypotheses that
736 surpass the global 5% or 10% significance level under strict error control requirements.
737 FWER³⁹, k-familywise error rate⁴¹ (k-FWER), and false discovery rate³⁹ (FDR) analyses
738 are applied (Methods). We note that all three metrics heavily favor the null. The presence
739 of local tests that reject the null therefore represents a strong confirmation of the
740 significance of those local tests, as those local tests are so highly significant that they can
741 withstand the stricter multiple testing error control criteria.

742

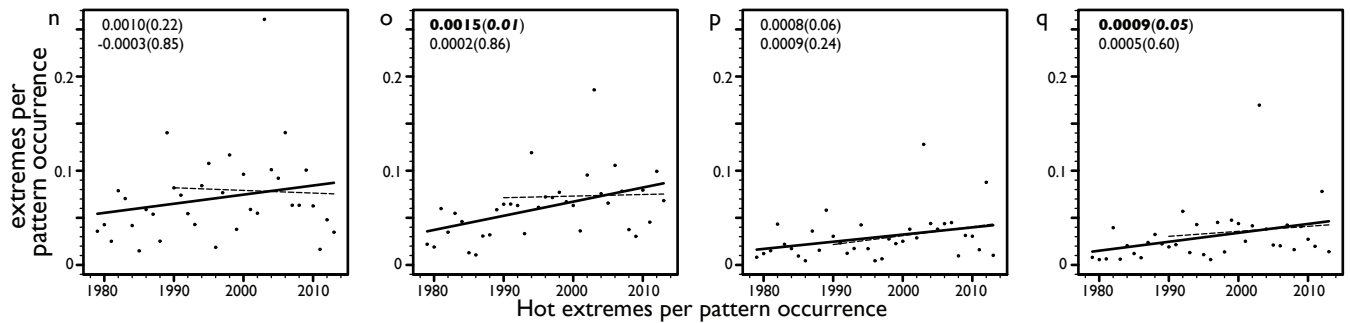
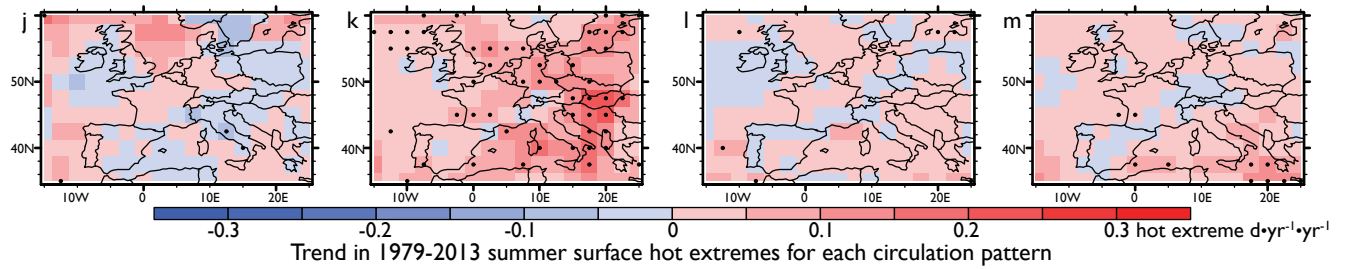
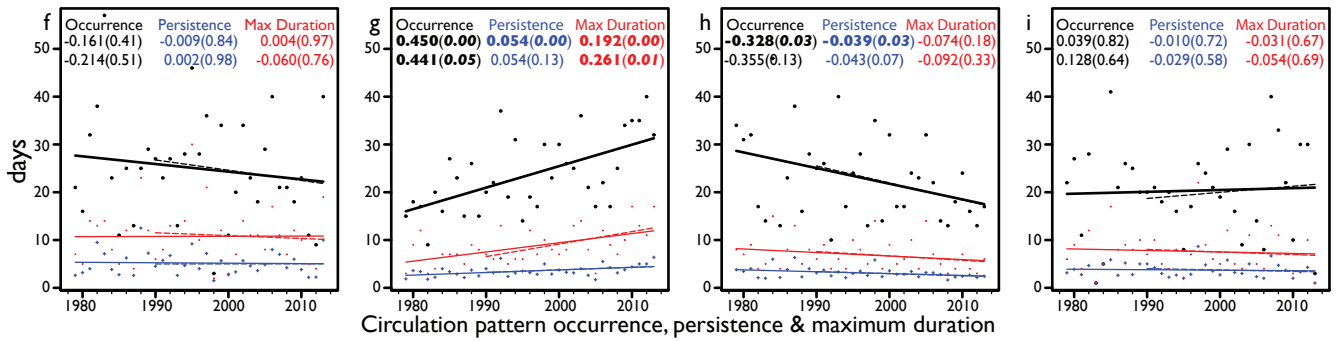
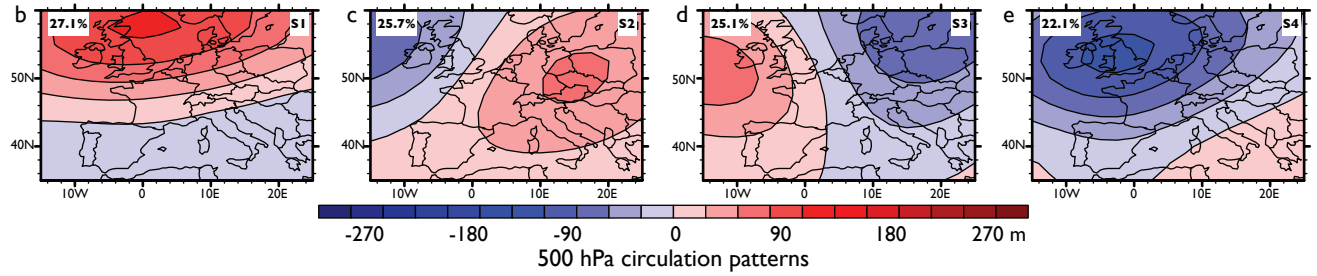
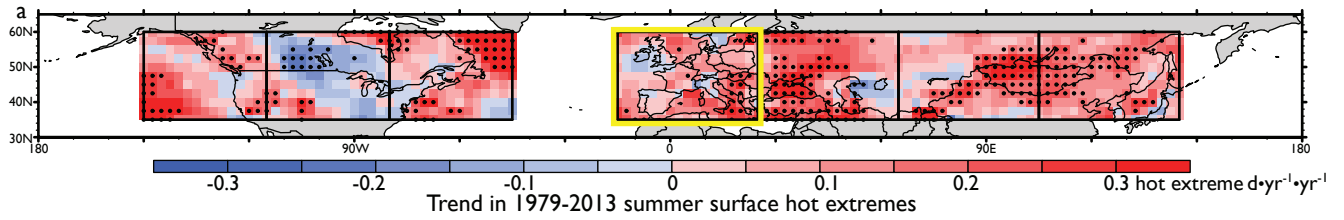
743 **Extended Data Table 2 | Quantitative partitioning of temperature extreme trends**
744 **for select SOM analyses.** Trends are partitioned for **a** Europe, **b** western Asia, and **c**
745 eastern North America sat-era summer hot extremes; **d** central Asia ice-era winter cold
746 extremes; **e** eastern North America sat-era autumn hot extremes; and **f** eastern Asia sat-
747 era autumn cold extremes. From the left column moving right, (1) SOM node number, (2)
748 trend in pattern occurrence [$[\text{“pat-occ”d}\cdot\text{yr}^{-1}\cdot\text{yr}^{-1}]$], (3) mean pattern occurrence for the
749 period [$[\text{“pat-occ”d}\cdot\text{yr}^{-1}]$], (4) trend in temperature extremes per pattern occurrence
750 (intensity of extreme occurrence) [$[\text{“ext-occ”d}\cdot\text{“pat-occ”d}^{-1}\cdot\text{yr}^{-1}\cdot\text{yr}^{-1}]$], (5) mean
751 temperature extreme per pattern occurrence [$[\text{“ext-occ”d}\cdot\text{“pat-occ”d}^{-1}\cdot\text{yr}^{-1}]$], (6) trend in
752 the dynamic influences [$[\text{“ext-occ”d}\cdot\text{yr}^{-1}\cdot\text{yr}^{-1}]$], (7) trend in the thermodynamic influences
753 [$[\text{“ext-occ”d}\cdot\text{yr}^{-1}\cdot\text{yr}^{-1}]$], (8) trend in the interaction of dynamic and thermodynamic
754 influences [$[\text{“ext-occ”d}\cdot\text{yr}^{-1}\cdot\text{yr}^{-1}]$], (9) the total trend in extreme occurrence for each SOM
755 pattern [$[\text{“ext-occ”d}\cdot\text{yr}^{-1}\cdot\text{yr}^{-1}]$], (10) the percent of the total trend in extreme occurrences
756 that occur during each pattern (pattern trend percentages sum to 100%, meaning
757 contributions from individual SOM patterns can be either positive or negative; that is,
758 trend percentages greater than 100% indicate that other circulation patterns provide
759 negative contributions), (11) the percent of column 10 that is due to dynamic influences,
760 (12) the percent of column 10 that is due to thermodynamic influences, and (13) the
761 percent of column 10 that is due to interactive influences (dynamic, thermodynamic, and
762 interactive influence percentages for individual SOM patterns sum to 100%, meaning

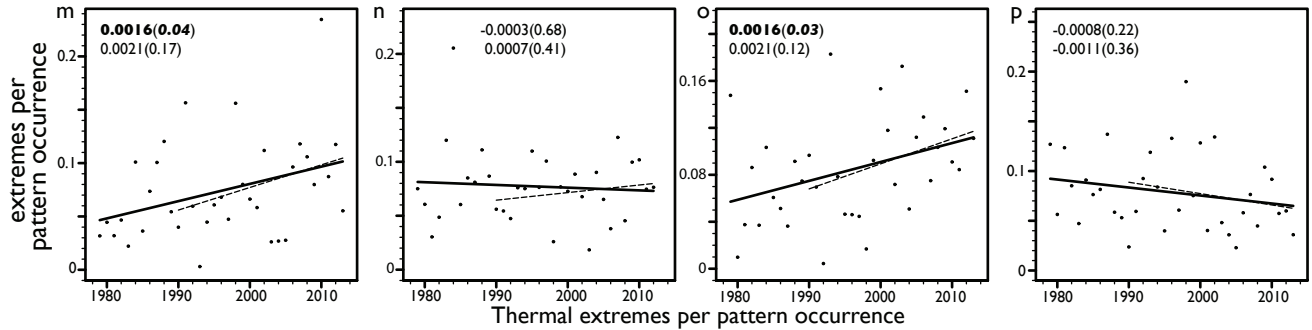
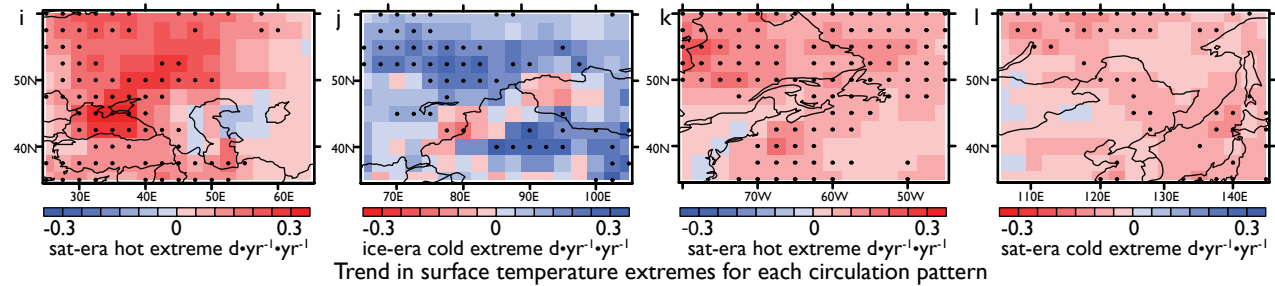
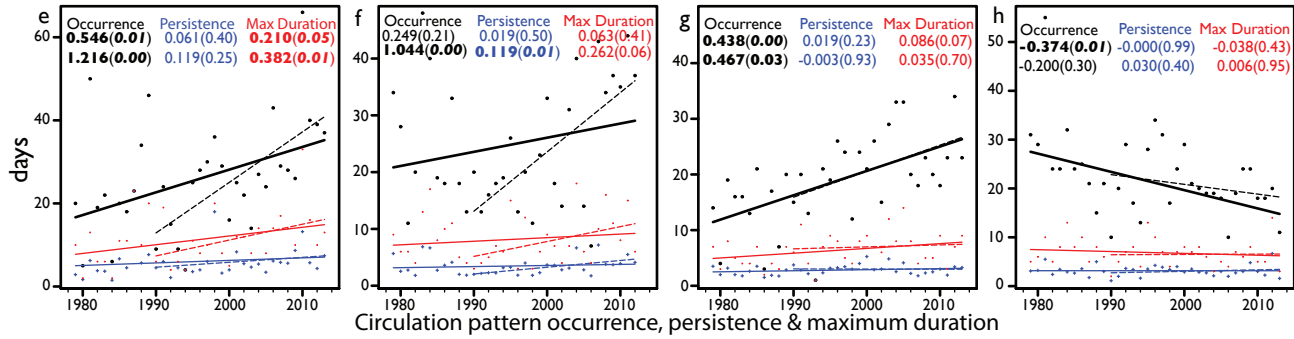
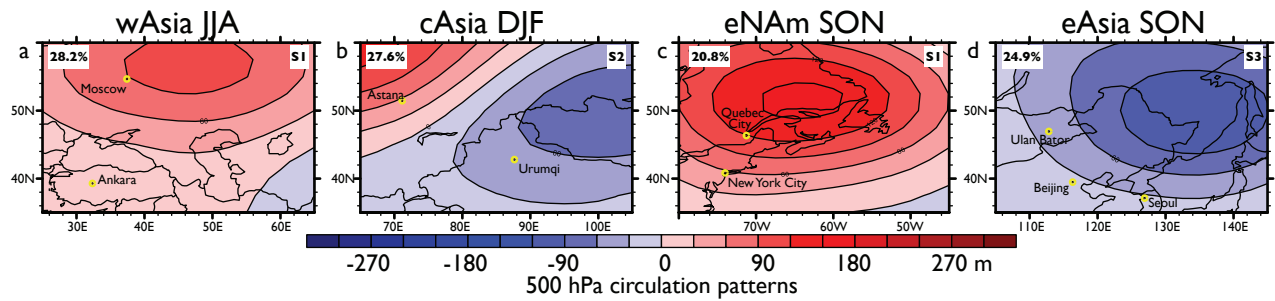
763 contributions from individual influences can be either positive or negative). The overall
764 trends for the domain are presented below the individual SOM rows. All data are sourced
765 from the NCEP-DOE-R2 reanalysis³³.

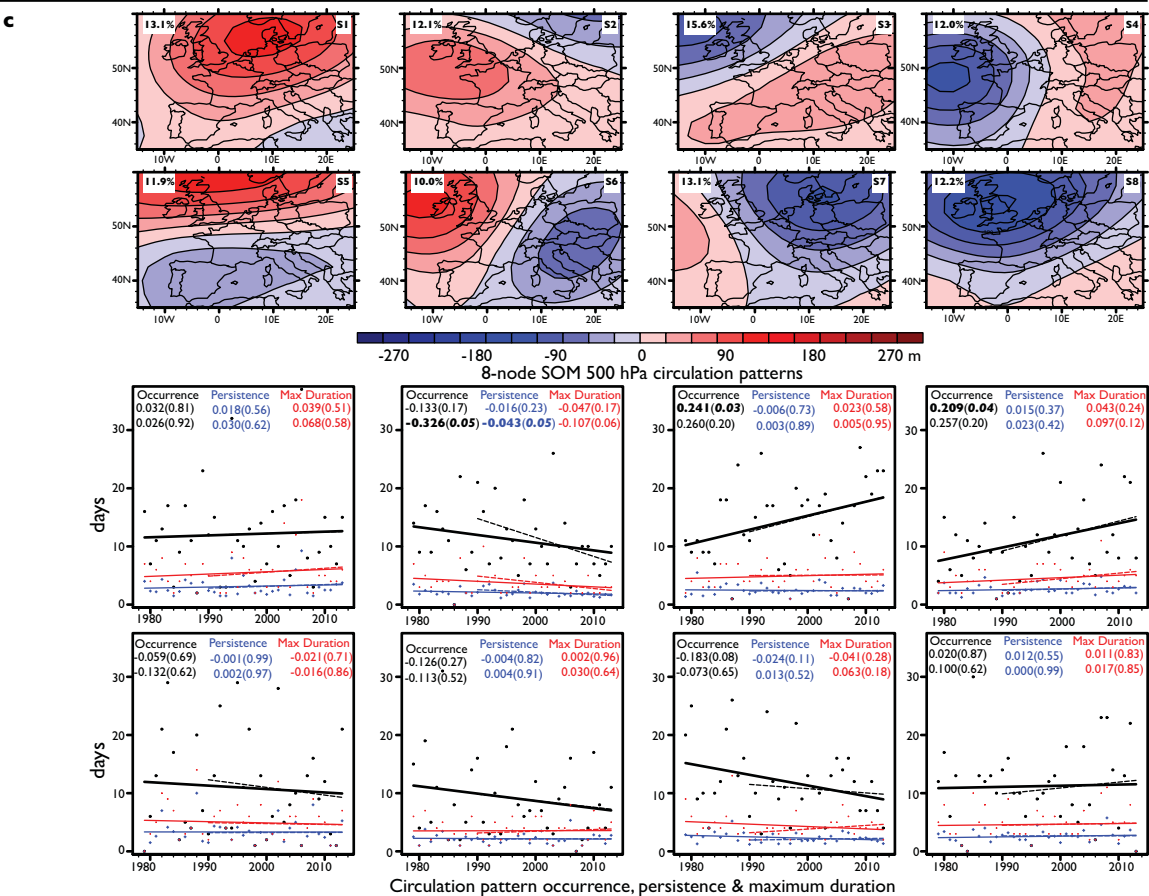
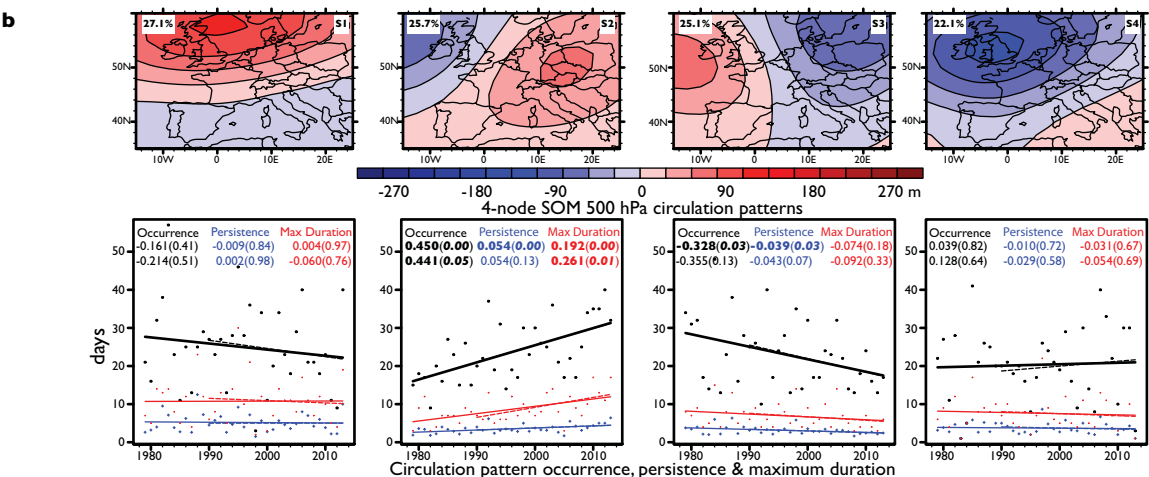
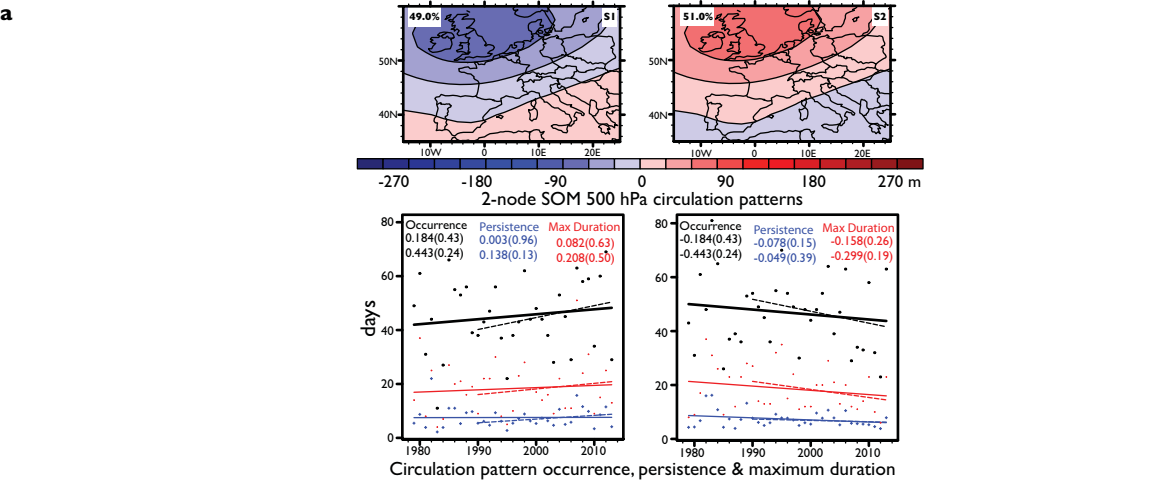


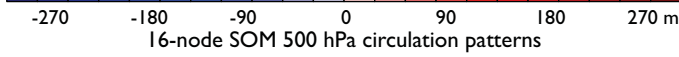
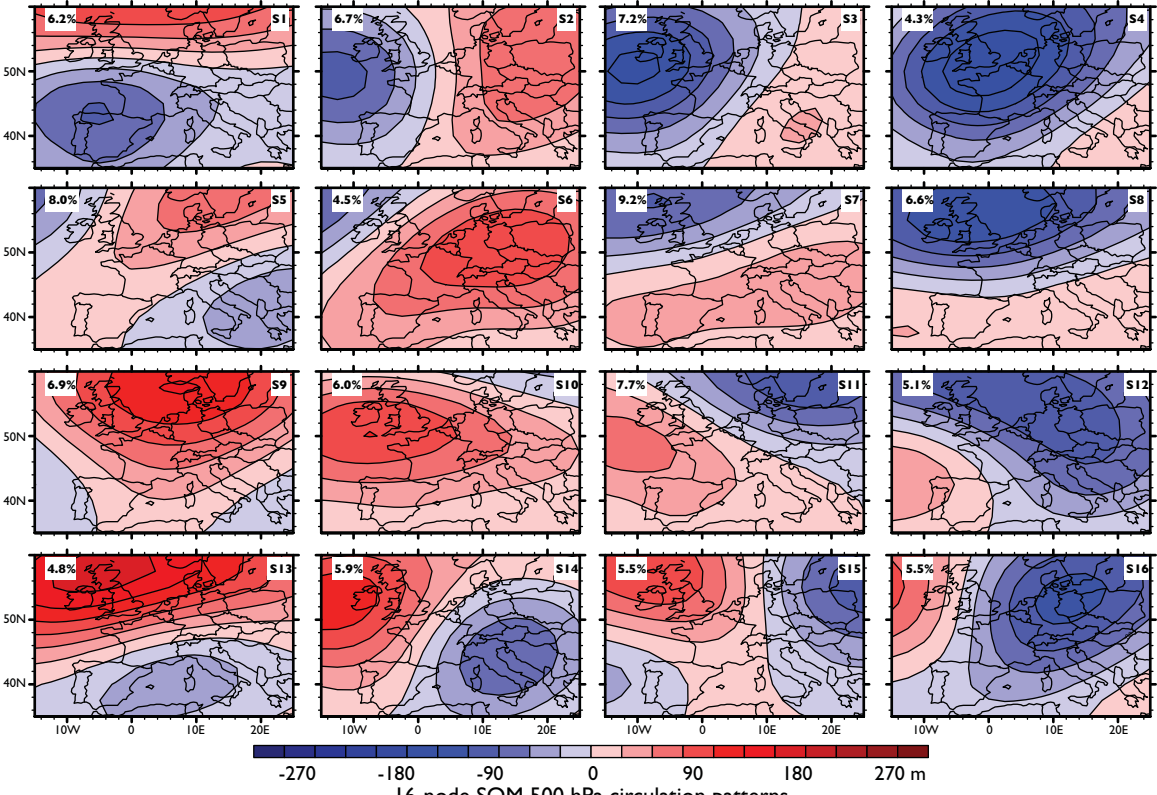
		DJF				MAM				JJA				SON								
		05	95	O	P	M	05	95	O	P	M	05	95	O	P	M	05	95	O	P	M	
Euro (Europe)	sat						-		+			-	+	+	+							
	ice	+										-	+			+	-	+				-
wAsia (western Asia)	sat						+					-	+	+		-	+				-	
	ice		+	-	+	+	-	+				-	+	+		+	-	+			+	
cAsia (central Asia)	sat						-	+				-					-					
	ice	+	-	+	+		-	+				-	+				-					
eAsia (eastern Asia)	sat											-	+				-	+			+	
	ice	+	-				+	-				-	+				-	+				
wNAM (western N. America)	sat		-				+															-
	ice		-				+	-													-	+
cNAM (central N. America)	sat	-					+					-					-				+	
	ice	-										-	+				-	+				
eNAM (eastern N. America)	sat	-					-					-		+	-	+	-	+			+	
	ice	-	+				-					-	+	+	-	-	-	+			+	

500 hPa Circulation Pattern Occurrence (O),	robust change
Persistence (P) & Maximum Duration (M)	equivocal
Reanalyses Surface Temperature Extremes Cold (05) & Hot (95)	cooling equivocal warming
1979-2013 (sat) & 1990-2013 (ice) Trends	(+) positive (-) negative

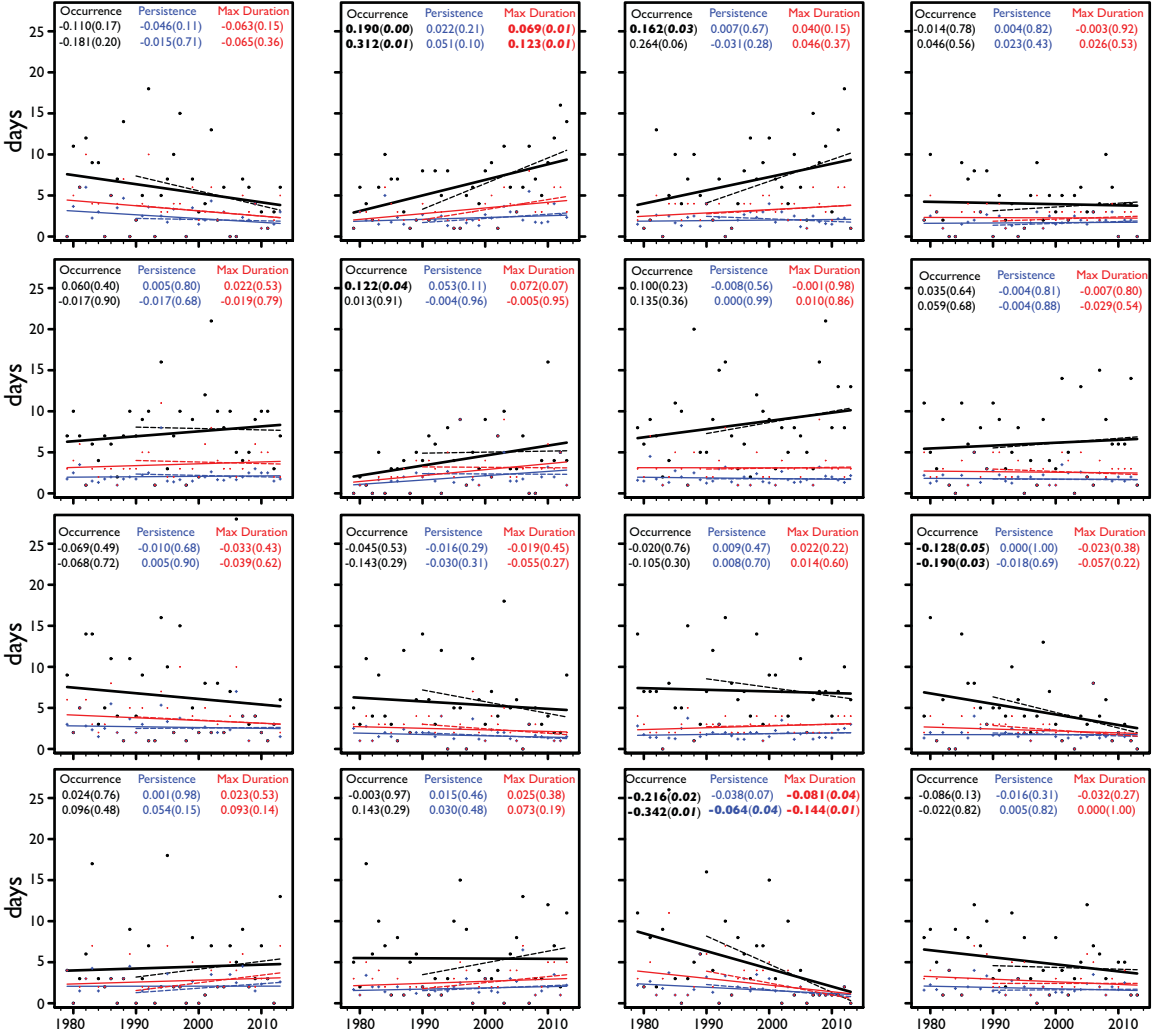




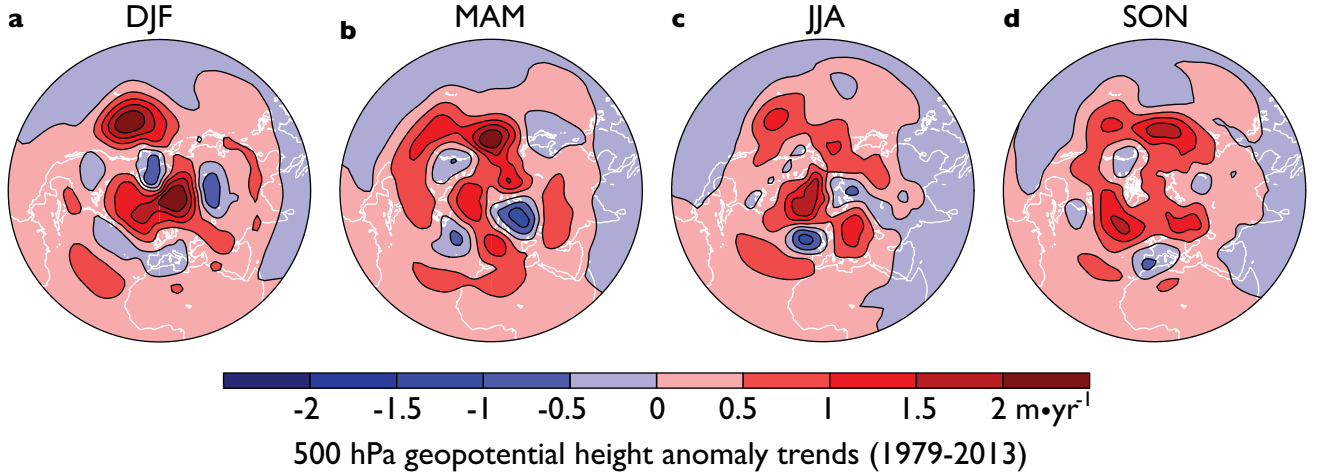




16-node SOM 500 hPa circulation patterns



Circulation pattern occurrence, persistence & maximum duration



e

1979-2013 Trends in area-weighted geopotential height anomalies ($\text{m}\cdot\text{yr}^{-1}$)				
	DJF	MAM	JJA	SON
N.Hemisphere	0.343	0.304	0.232	0.293
Euro	0.033	0.708	0.221	0.053
wAsia	0.467	0.361	0.656	0.585
cAsia	-0.209	0.491	0.130	0.151
eAsia	0.134	0.100	0.439	0.551
wNA	0.593	0.314	0.438	0.386
cNA	0.236	0.409	0.207	0.550
eNA	0.337	0.319	0.527	0.818

f

Trend Removed	Euro-JJA-1979-2013											
	A			C-A			A-C			C		
	OCC	PER	DUR	OCC	PER	DUR	OCC	PER	DUR	OCC	PER	DUR
None	-0.161	-0.009	0.004	0.45	0.054	0.192	-0.328	-0.039	-0.074	0.039	-0.01	-0.031
N.Hemisphere	-0.196	-0.013	-0.002	0.42	0.05	0.173	-0.33	-0.037	-0.067	0.105	-0.004	-0.005

g

Trend Removed	wAsia-JJA-1979-2013											
	A			C-A			A-C			C		
	OCC	PER	DUR	OCC	PER	DUR	OCC	PER	DUR	OCC	PER	DUR
None	0.546	0.061	0.21	-0.366	-0.04	-0.135	0.057	0.005	-0.02	-0.237	0.031	0.035
N.Hemisphere	0.352	0.034	0.127	-0.301	-0.03	-0.126	0.114	0.004	0	-0.165	0.036	0.046

h

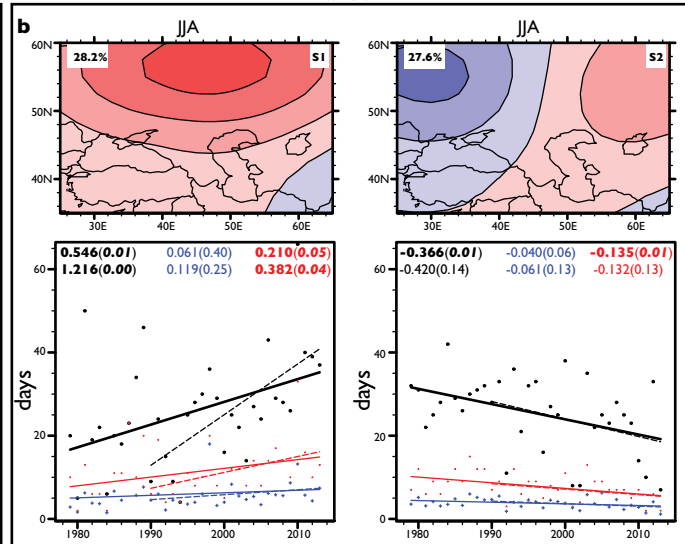
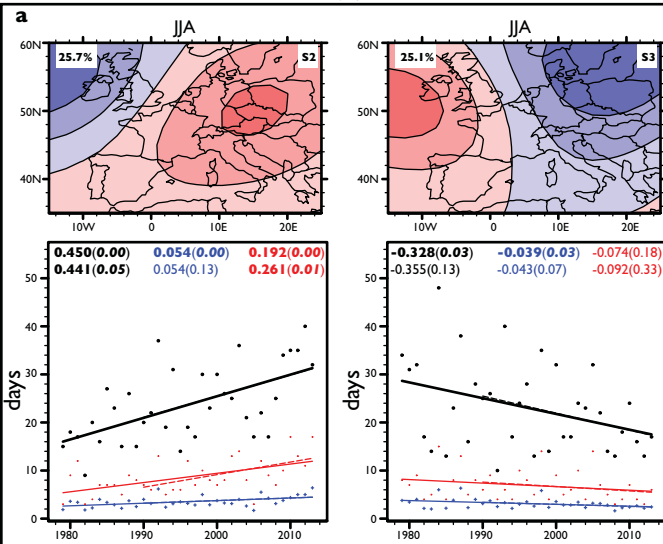
Trend Removed	eNA-SO											
	A			A-C			C-A			C		
	OCC	PER	DUR	OCC	PER	DUR	OCC	PER	DUR	OCC	PER	DUR
None	0.438	0.019	0.086	-0.285	-0.011	-0.063	0.097	0.013	-0.037	-0.25	-0.007	0.003
N.Hemisphere	0.366	0.017	0.075	-0.266	-0.005	-0.055	0.091	0.01	-0.041	-0.19	-0.002	0.003

i

Trend Removed	eAsia-SO											
	A-C			A			C			C-A		
	OCC	PER	DUR	OCC	PER	DUR	OCC	PER	DUR	OCC	PER	DUR
None	-0.114	-0.01	0.015	0.366	0.025	0.091	-0.374	0	-0.038	0.122	0.02	0.049
N.Hemisphere	-0.101	-0.003	0.015	0.217	0.01	0.036	-0.229	0.034	-0.017	0.113	0.023	0.049

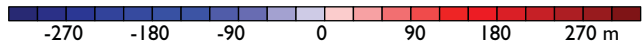
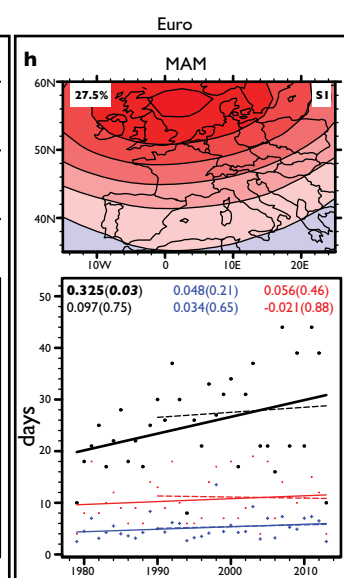
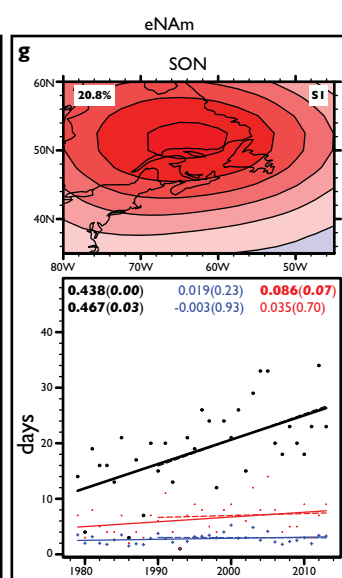
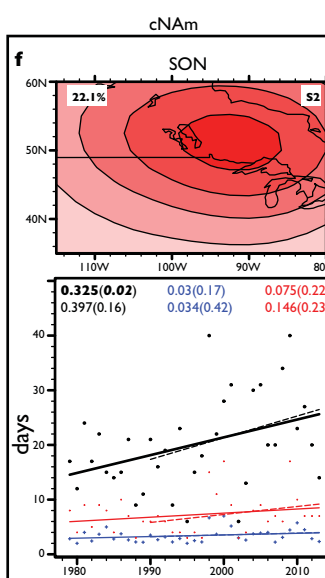
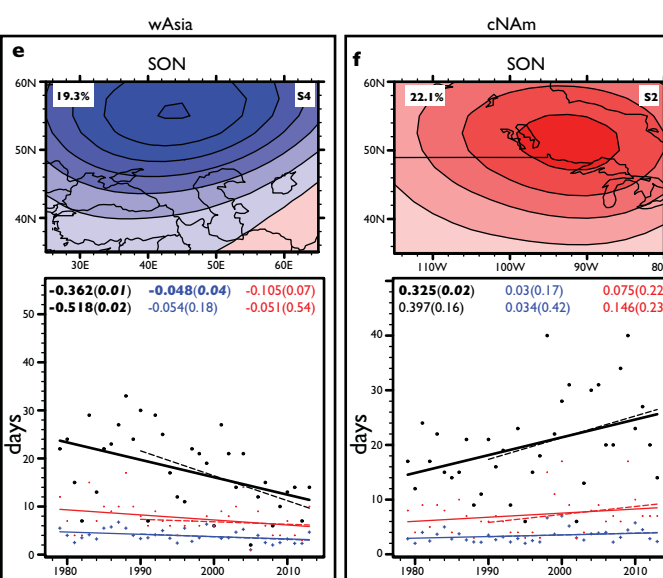
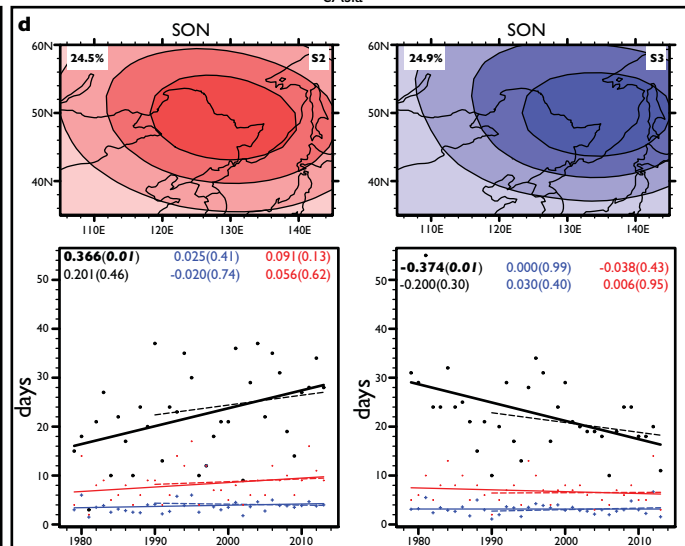
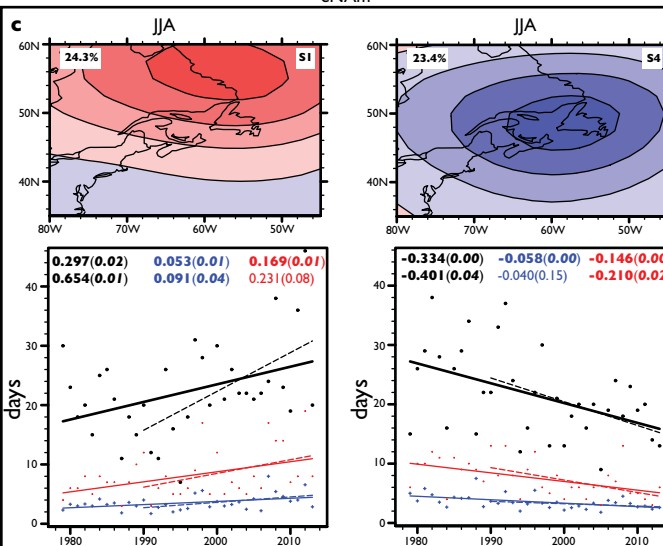
j

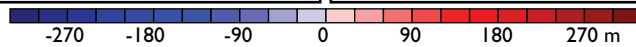
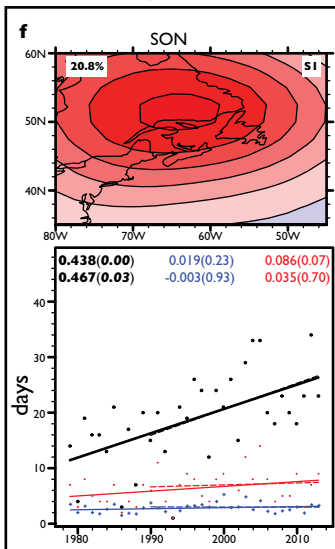
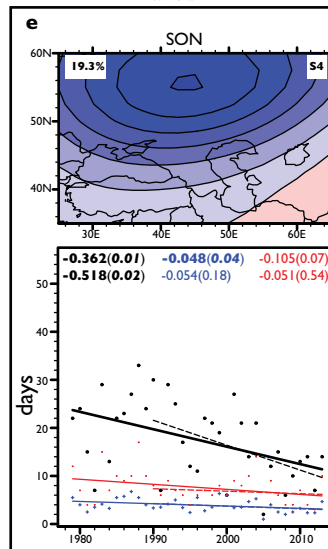
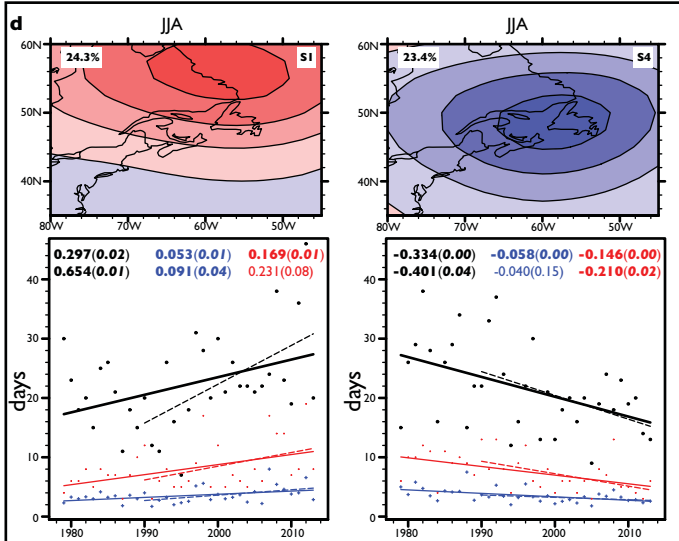
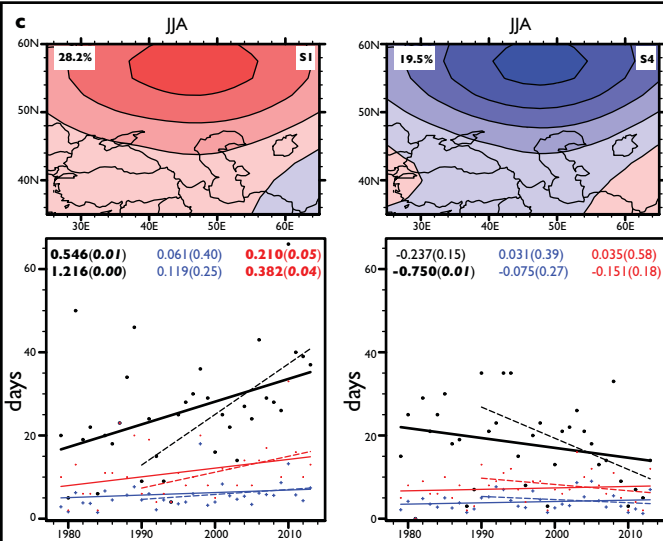
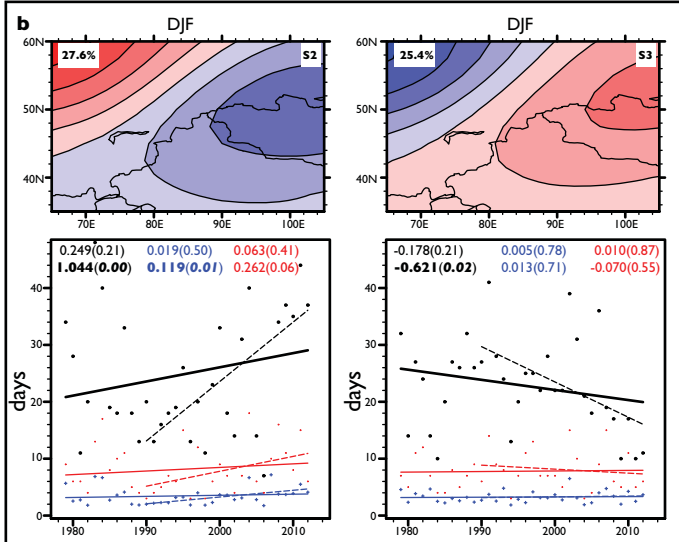
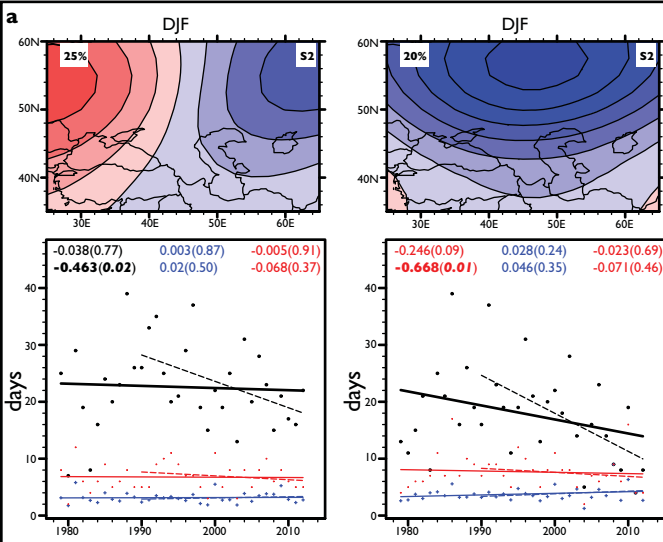
Trend Removed	cAsia-DJF-1990-2013											
	A			A-C			C-A			C		
	OCC	PER	DUR	OCC	PER	DUR	OCC	PER	DUR	OCC	PER	DUR
None	-0.127	0.03	0.127	1.044	0.119	0.262	-0.621	0.013	-0.07	-0.296	-0.005	-0.042
N.Hemisphere	-0.169	0.037	0.103	1.105	0.144	0.319	-0.701	0.021	0.004	-0.235	0.004	0.006

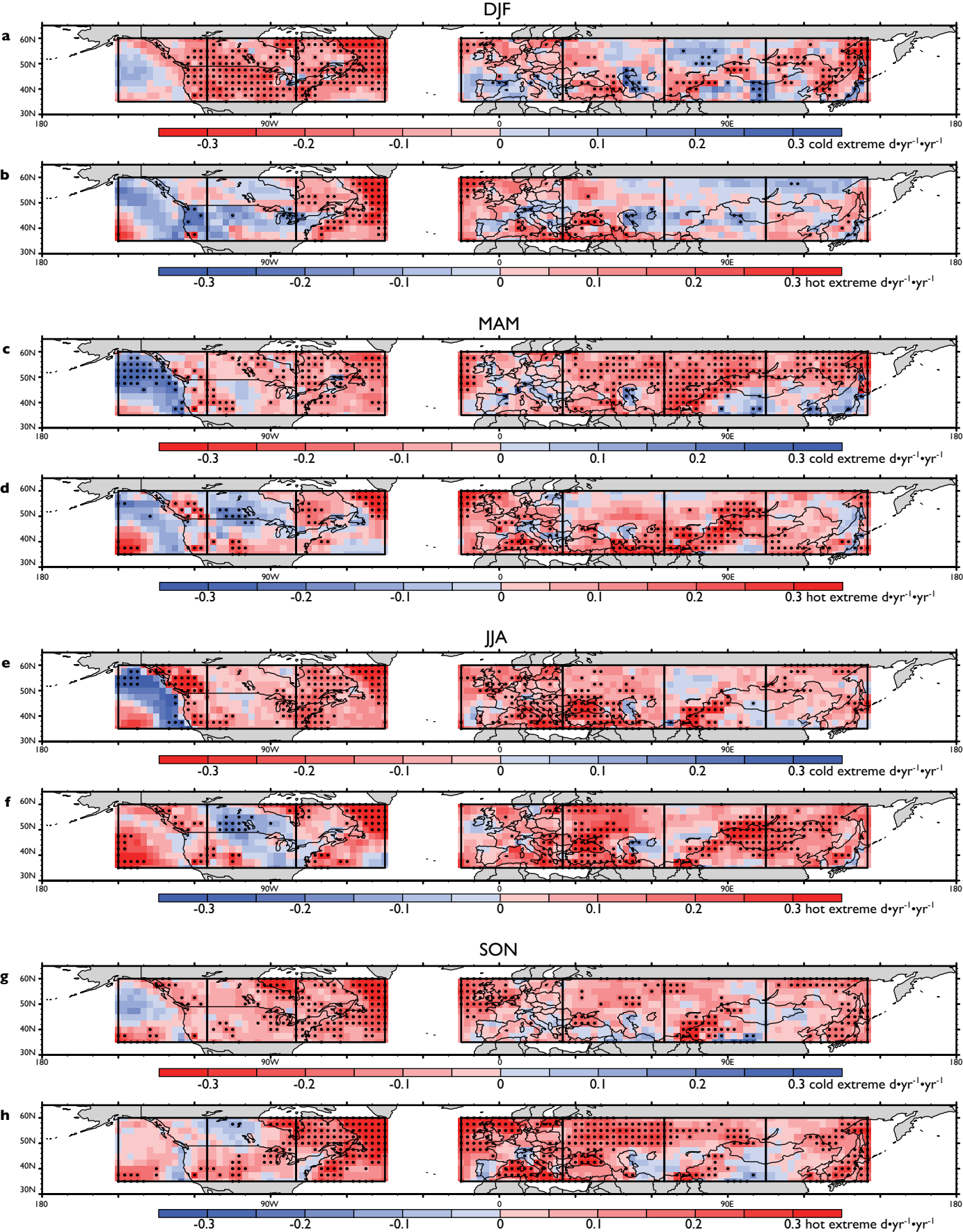


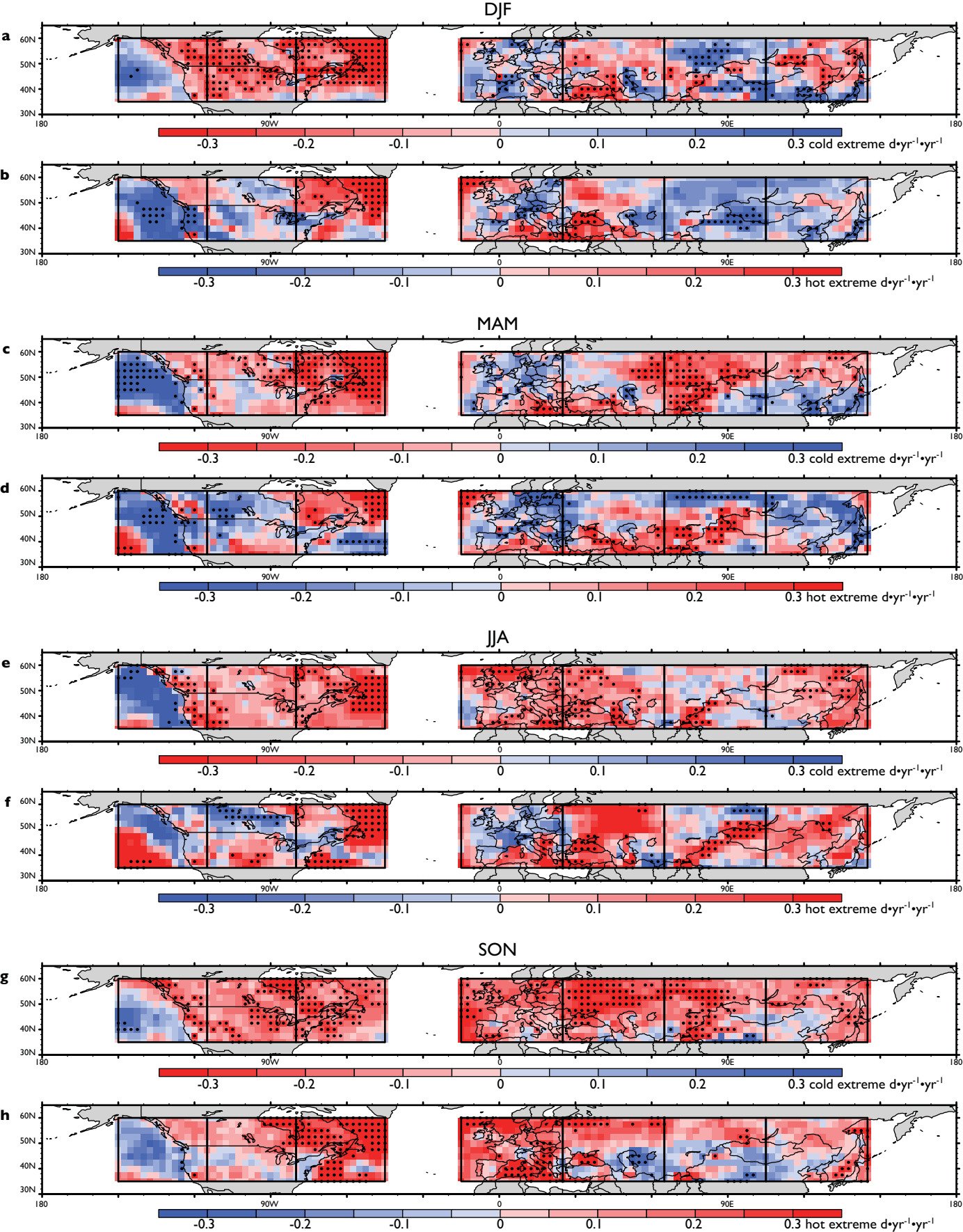
eNAM

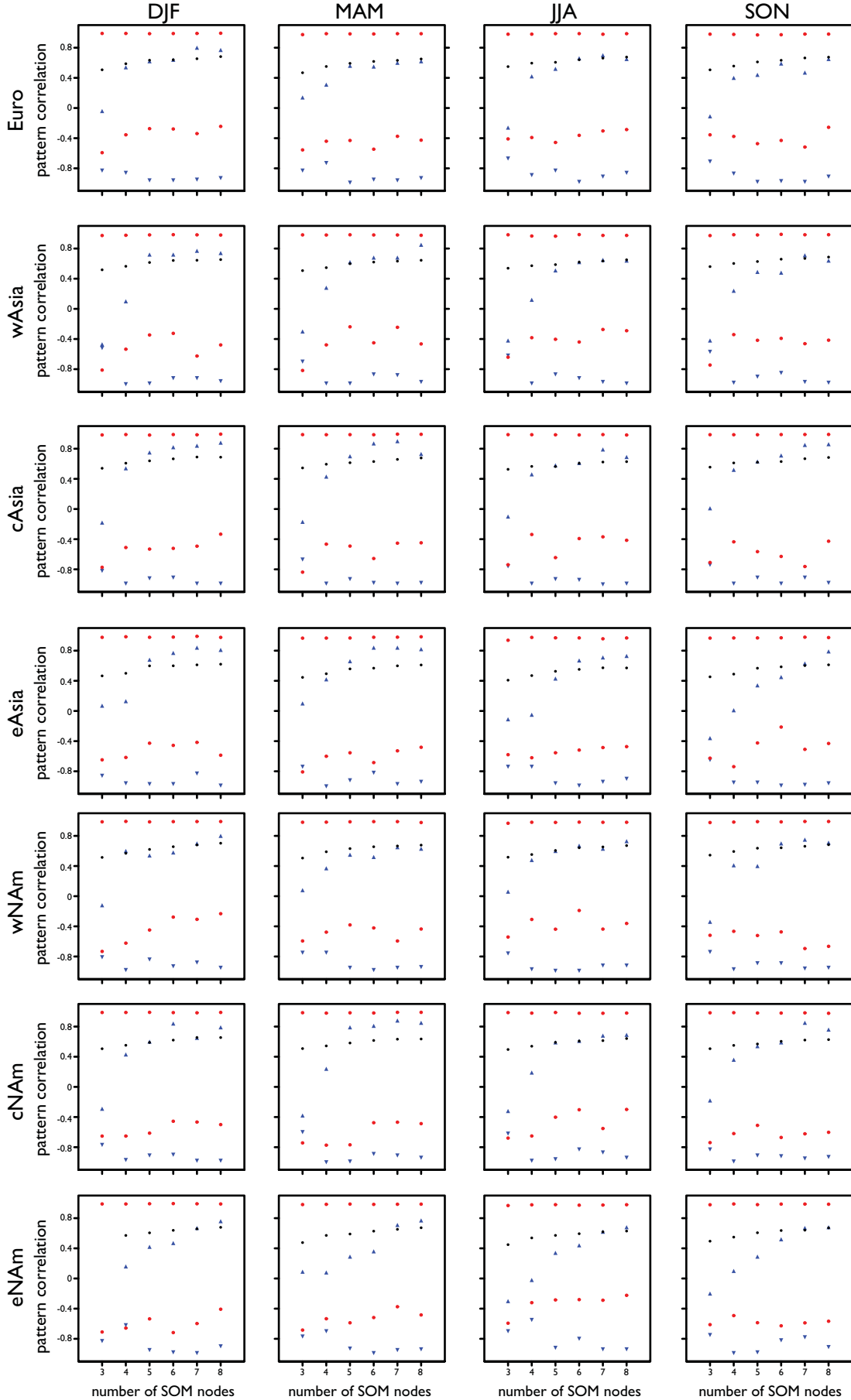
eAsia











● Max/Min pattern correlation of daily geopotential height anom. fields with matching SOM node pattern
 ● Mean pattern correlation of all daily geopotential height anom. fields with matching SOM node patterns
 ▲ Maximum SOM pattern to SOM pattern correlation
 ▼ Minimum SOM pattern to SOM pattern correlation

a

Statistically Significant Trends (p<0.05)							
	n	sat-era			ice-era		
		occ	per	dur	occ	per	dur
Linear Regression Analysis							
NCAR/NCEP-R1	112	17	6	7	15	10	9
NCEP-DOE-R2	112	16	5	7	13	8	9
ERA-Interim	112	16	6	10	14	9	9
Box-Cox Transformation Analysis							
NCAR/NCEP-R1	112	15	9	8	16	9	10
NCEP-DOE-R2	112	15	6	7	16	10	10
ERA-Interim	112	16	8	12	14	9	11

b

Anderson Darling Test for Normality							
	n	sat-era			ice-era		
		occ	per	dur	occ	per	dur
Original Data							
NCAR/NCEP-R1	112	103	47	56	102	76	68
NCEP-DOE-R2	112	102	57	58	102	74	70
ERA-Interim	112	99	62	49	105	76	65
Original Data with FWER Multiple Hypothesis Testing							
NCAR/NCEP-R1	112	112	102	102	112	103	107
NCEP-DOE-R2	112	112	100	103	112	107	109
ERA-Interim	112	112	100	102	112	104	106
Box-Cox Transformed Data							
NCAR/NCEP-R1	112	110	109	110	109	110	112
NCEP-DOE-R2	112	111	110	110	110	111	112
ERA-Interim	112	110	111	109	111	109	108
Box-Cox Transformed Data with FWER Multiple Hypothesis Testing							
NCAR/NCEP-R1	112	112	112	112	112	112	112
NCEP-DOE-R2	112	112	112	112	112	112	112
ERA-Interim	112	112	112	112	112	112	112

c

Multiple Hypothesis Testing							
Control Type	Level	sat-era			ice-era		
		occ	per	dur	occ	per	dur
NCAR/NCEP-R1							
FWER	5%	2	0	0	0	1	0
	10%	2	0	1	1	1	0
k-FWER	5%	4	1	2	1	2	0
	10%	7	2	3	4	2	2
FDR	5%	0	0	0	0	0	0
	10%	2	0	0	0	0	0
NCEP-DOE-R2							
FWER	5%	2	0	0	0	1	0
	10%	2	0	1	0	1	0
k-FWER	5%	2	1	2	2	2	0
	10%	5	2	4	5	3	0
FDR	5%	0	0	0	0	0	0
	10%	2	0	0	0	0	0
ERA-Interim							
FWER	5%	0	0	1	0	0	0
	10%	1	0	1	0	0	0
k-FWER	5%	3	2	2	2	0	1
	10%	7	2	2	5	3	3
FDR	5%	0	0	0	0	0	0
	10%	0	0	0	0	0	0

a **1979-2013 Europe JJA Hot Extreme Partitioning**

	Pat occ trend	Mean pat occ	T95 per pat occ trend	Mean T95 per pat occ	Dyn trend	Thermo trend	Inter trend	Total trend	Percent of trend	Percent dynamic	Percent thermo	Percent inter
SOM1	-0.16	24.94	0.001	0.07	-0.01	0.02	0.00	0.01	10.1	-112.0	237.9	-25.9
SOM2	0.45	23.66	0.002	0.06	0.03	0.04	0.00	0.06	61.5	44.3	57.3	-1.6
SOM3	-0.33	23.09	0.001	0.03	-0.01	0.02	0.00	0.01	8.7	-109.3	200.9	8.4
SOM4	0.04	20.31	0.001	0.03	0.00	0.02	0.00	0.02	19.7	5.9	96.6	-2.5
Overall:					0.01	0.10	0.00	0.10				

b **1979-2013 Western Asia JJA Hot Extreme Partitioning**

	Pat occ trend	Mean pat occ	T95 per pat occ trend	Mean T95 per pat occ	Dyn trend	Thermo trend	Inter trend	Total trend	Percent of trend	Percent dynamic	Percent thermo	Percent inter
SOM1	0.55	25.94	0.002	0.07	0.04	0.04	0.03	0.11	70.3	36.5	37.8	25.7
SOM2	-0.37	25.40	0.001	0.05	-0.02	0.04	0.00	0.02	11.8	-92.3	198.0	-5.7
SOM3	0.06	22.69	0.001	0.03	0.00	0.02	-0.01	0.02	12.0	9.9	122.3	-32.1
SOM4	-0.24	17.97	0.001	0.03	-0.01	0.02	-0.01	0.01	5.9	-72.2	240.8	-68.6
Overall:					0.02	0.12	0.01	0.16				

c **1979-2013 Eastern North America JJA Hot Extreme Partitioning**

	Pat occ trend	Mean pat occ	T95 per pat occ trend	Mean T95 per pat occ	Dyn trend	Thermo trend	Inter trend	Total trend	Percent of trend	Percent dynamic	Percent thermo	Percent inter
SOM1	0.30	22.31	0.002	0.07	0.02	0.04	0.01	0.07	51.4	29.9	56.8	13.3
SOM2	-0.02	21.63	0.001	0.05	0.00	0.02	0.00	0.02	13.1	-5.1	114.4	-9.3
SOM3	0.05	26.51	0.001	0.04	0.00	0.04	0.00	0.03	26.7	6.8	106.7	-13.6
SOM4	-0.33	21.54	0.001	0.04	-0.01	0.03	0.00	0.01	8.7	-105.6	234.8	-29.1
Overall:					0.01	0.12	0.00	0.13				

d **1990-2013 Central Asia DJF Cold Extreme Partitioning**

	Pat occ trend	Mean pat occ	T05 per pat occ trend	Mean T05 per pat occ	Dyn trend	Thermo trend	Inter trend	Total trend	Percent of trend	Percent dynamic	Percent thermo	Percent inter
SOM1	-0.13	21.04	0.001	0.04	0.00	0.01	0.00	0.01	9.0	-79.0	177.8	1.3
SOM2	1.04	24.61	0.001	0.07	0.08	0.02	0.01	0.10	149.6	74.6	18.1	7.2
SOM3	-0.62	22.87	0.000	0.02	-0.01	0.01	-0.01	-0.01	-21.3	98.0	-45.4	47.4
SOM4	-0.30	21.74	-0.001	0.05	-0.02	-0.02	0.01	-0.03	-37.2	59.7	68.2	-27.8
Overall:					0.04	0.02	0.01	0.07				

e **1979-2013 Eastern North America SON Hot Extreme Partitioning**

	Pat occ trend	Mean pat occ	T95 per pat occ trend	Mean T95 per pat occ	Dyn trend	Thermo trend	Inter trend	Total trend	Percent of trend	Percent dynamic	Percent thermo	Percent inter
SOM1	0.44	18.89	0.002	0.08	0.04	0.03	0.00	0.07	37.0	51.7	42.5	5.8
SOM2	-0.29	28.40	0.001	0.03	-0.01	0.03	0.00	0.02	10.5	-45.3	156.9	-11.6
SOM3	0.10	25.91	0.003	0.06	0.01	0.07	0.01	0.08	43.8	6.6	86.3	7.1
SOM4	-0.25	17.80	0.002	0.03	-0.01	0.03	0.00	0.02	8.7	-44.1	161.9	-17.8
Overall:					0.03	0.16	0.00	0.19				

f **1979-2013 East Asia SON Cold Extreme Partitioning**

	Pat occ trend	Mean pat occ	T05 per pat occ trend	Mean T05 per pat occ	Dyn trend	Thermo trend	Inter trend	Total trend	Percent of trend	Percent dynamic	Percent thermo	Percent inter
SOM1	-0.11	19.43	-0.001	0.05	-0.01	-0.02	0.01	-0.02	18.4	40.2	152.7	-92.9
SOM2	0.37	22.29	-0.001	0.03	0.01	-0.01	0.00	0.00	0.8	-1637.5	1844.1	-106.5
SOM3	-0.37	22.69	-0.001	0.08	-0.03	-0.02	0.00	-0.05	62.5	56.5	35.0	8.4
SOM4	0.12	26.60	-0.001	0.04	0.00	-0.02	0.00	-0.02	18.3	-31.2	119.7	11.5
Overall:					-0.02	-0.07	0.01	-0.08				